

**M A S A R Y K O V A
U N I V E R Z I T A**

**Přírodovědecká fakulta
Ústav teoretické fyziky a astrofyziky**

Bakalářská práce

BRNO 2025

BARBORA MIKLOŠOVÁ

**MASARYKOVA
UNIVERZITA**

**Zkoumání
radiomechanické zpětné
vazby aktivních
galaktických jader pomocí
vícedutinových systémů**

Bakalářská práce

Barbora Miklošová

Vedoucí práce: Mgr. Tomáš Plšek

Brno 2025

Bibliografický záznam

Autor:	Barbora Miklošová Přírodovědecká fakulta, Masarykova univerzita Ústav teoretické fyziky a astrofyziky
Název práce:	Zkoumání radiomechanické zpětné vazby aktivních galaktických jader pomocí vícedutinových systémů
Studijní program:	Fyzika
Studijní obor:	Astrofyzika
Vedoucí práce:	Mgr. Tomáš Plšek
Akademický rok:	2024/2025
Počet stran:	xvii + 60
Klíčová slova:	zpětná vazba aktivních galaktických jader; rentgenové dutiny; vícedutinové systémy; rentgenová observatoř Chandra; výkony jetů; obří eliptické galaxie

Bibliographic Entry

Author: Barbora Miklošová
Faculty of Science, Masaryk University
Department of Theoretical Physics and Astrophysics

Title of Thesis: Probing the radio-mechanical AGN feedback using multi-cavity systems

Degree Programme: Physics

Field of Study: Astrophysics

Supervisor: Mgr. Tomáš Plšek

Academic Year: 2024/2025

Number of Pages: xvii + 60

Keywords: AGN feedback; X-ray cavities; multi-cavity systems; Chandra X-ray Observatory; jet power; giant ellipticals

Abstrakt

Tato studie se zaměřuje na radiomechanickou zpětnou vazbu aktivních galaktických jader v blízkých obřích eliptických galaxiích, které vykazují více generací rentgenových dutin. Zpracováním a analýzou dat z rentgenového dalekohledu *Chandra* pro vybraný vzorek galaxií kvantifikujeme výkon výtrysků, které vytvářejí rentgenové dutiny a přispívají k ohřevu horké atmosféry. Představujeme vylepšený postup pro odhad stáří dutin a energie, která je v nich obsažena. Dále hodnotíme vliv inklinace na naše měření a zkoumáme její potenciál ovlivnit pozorované trendy výkonu výtrysků v našich systémech. Zjistili jsme, že inklinace může vést k nadhodnocení výkonu jetu až o řád. Také jsme zjistili, že projekční efekty jsou výraznější u zploštělých dutin a u těch, které se nacházejí dále od centra. Navíc u systému s výrazně nevyrovnanými generacemi dutin zkoumáme možné vysvětlení této nevyrovnanosti.

Abstract

This study focuses on radio-mechanical feedback of active galactic nuclei in nearby giant elliptical galaxies that showcase multiple generations of X-ray cavities. By processing and analysing data from *Chandra X-ray Observatory* for a selected sample of galaxies, we quantify the jet powers excavating the X-ray cavities that contribute to the heating of the X-ray atmospheres. We present an improved procedure for estimating cavity ages and the energy they encompass. We also assess the impact of inclination on our measurements and probe its potential to shift the observed trends in jet powers in our systems. We find that inclination can lead to the jet power overestimation by up to an order of magnitude. Moreover, we find that projection effects are more significant for oblate cavities, as well as for those that are further away from the centre. For a system with significantly misaligned cavity generations, we also examine potential explanations for the misalignment.

ZADÁNÍ
BAKALÁŘSKÉ PRÁCE

Akademický rok: 2024/2025

Ústav: Ústav teoretické fyziky a astrofyziky

Studentka: Barbora Miklošová

Program: Fyzika

Specializace: Astrofyzika

Ředitel ústavu PŘF MU Vám ve smyslu Studijního a zkušebního řádu MU určuje bakalářskou práci s názvem:

Název práce: Zkoumání radiomechanické zpětné vazby aktivních galaktických jader pomocí vícedutinových systémů

Název práce anglicky: Probing the radio-mechanical AGN feedback using multi-cavity systems

Jazyk práce: angličtina

Oficiální zadání:

Estimating the mechanical power of relativistic jets emanating from active galactic nuclei (AGN) and inflating X-ray cavities into hot atmospheres of elliptical galaxies and galaxy clusters has been a hot topic in X-ray astronomy for the past 30 years. In the current approach, jet powers are derived from sizes of X-ray cavities, which are simplified to have ellipsoidal shapes and lie in the plane of the sky, with their ages determined using additional simplifying assumptions.

The aim of the thesis is to perform a statistical study of the jet powers and enthalpies of X-ray cavities in multi-cavity systems. The student will compare the current approach of jet power estimation with a novel method leveraging machine learning techniques, take into account various possible jet re-orientation scenarios and inclination angles and properly estimate the timescale of cavity inflation. By comparing enthalpies and jet powers of several generations of X-ray cavities for multiple systems, the thesis will hopefully shed more light on the process of jet power estimation, in particular, improving the estimates for previously detached X-ray cavities.

Vedoucí práce: Mgr. Tomáš Plšek

Konzultant: RNDr. Michal Zajaček, Dr. rer. nat.

Datum zadání práce: 1. 11. 2024

V Brně dne: 8. 4. 2025

Zadání bylo schváleno prostřednictvím IS MU.

Barbora Miklošová, 25. 11. 2024

Mgr. Tomáš Plšek, 26. 11. 2024

RNDr. Luboš Poláček, 4. 12. 2024

Pod'akovanie

V prvom rade sa chcem pod'akovať vedúcemu tejto práce, Mgr. Tomášovi Plškovi. Patrí mu vrúcna vd'aka za jeho dobrosrdečný a úprimný prístup, za nekonečné množstvo času, ktorý venoval tejto práci a hlavne trpezlivosť, ktorú so mnou mal. Ďalej sa chcem pod'akovať RNDr. Michalovi Zajačkovi, Dr. rer. nat. za čas strávený debátovaním precesie a s tým spojenými témami a za aktívny záujem o túto prácu.

Bez lásky, obety, a podpory, ktorá sa mi dostala od mojich milovaných rodičov, najlepšej sestry a celej rodiny, by som to len ťažko zvládla. Ďakujem, že ste mi verným útočiskom a bezpečným miestom, kam sa rada vraciam.

Obrovská vd'aka patrí mojim priateľom, zvlášť tým, ktorých mi dala vysoká škola. Čas s Vami bol vykúpením v chvíľach únavy a spoločný smiech bol liekom pre dušu.

Nakoniec sa chcem pod'akovať Tomu, na koho najviac zabúdam a ktorý ma stále sprevádza. Vd'aka Nemu je môj život *milosť za milosťou*.

Prohlášení

Prohlašuji, že jsem svoji bakalářskou práci vypracovala samostatně pod vedením vedoucího práce s využitím informačních zdrojů, které jsou v práci citovány.

Brno 13. května 2025

.....
Barbora Miklošová

Contents

Notations & abbreviations	xvii
Introduction	1
Chapter 1. Hot atmospheres	3
1.1 X-ray emission	4
1.2 Cooling flows	5
1.3 Cold gas	7
Chapter 2. AGN feedback & X-ray cavities	9
2.1 AGN feedback	9
2.2 X-ray cavities	11
2.2.1 Cavity timescales	12
2.2.2 Cavity energetics	13
2.3 Misalignments in multi-cavity systems	13
Chapter 3. Data analysis	15
3.1 Spectral analysis	15
3.2 Image analysis	17
3.3 Timescales	18
3.3.1 Timescale correction	18
3.3.2 Uncertainties in cavity ages	19
3.4 Jet powers	19
3.5 Inclination	20
3.5.1 Toy bubbles	20
3.5.2 Studied cavities	21
3.6 Misalignments	21
Chapter 4. Results	23
4.1 NGC 5813	24
4.2 NGC 5044	25
4.3 NGC 4649	27
4.4 NGC 4472	29
Chapter 5. Discussion	35
5.1 Individual galaxies	36

5.1.1 NGC 5813	36
5.1.2 NGC 5044	36
5.1.3 NGC 4649	38
5.1.4 NGC 4472	40
5.2 Toy model	41
Conclusion	45
Appendix	47
A Observations	47
B Cavity timescales and energetics	49
B.1 NGC 5813	49
B.2 NGC 5044	50
B.3 NGC 4649	51
B.4 NGC 4472	52
C Eddington efficiency	53
D Understanding the amount of jet power	53
References	55

***"Astronomy?
Impossible to understand
and madness to investigate."***

— Sophocles, 420 BC

Notations & abbreviations

The following section presents an overview of abbreviations and notation used throughout this work.

AGN	active galactic nuclei
gEs	giant elliptical galaxy
GGr	galaxy group
GC	galaxy cluster
SMBH	supper-massive black hole
(N)CC	(non)-cool-core
CCA	chaotic cold accretion
ICM	intra-cluster medium
CGM	circum-galactic medium
IGrM	intra-group medium
D	distance of a galaxy
d, d'	intrinsic and projected cavity distance, respectively
τ, τ'	intrinsic and radial elongation, respectively
t_{ss}	sound-speed timescale
t_{buo}	buoyancy timescale
t_{age}	corrected cavity age
R_l, R'_l	intrinsic and projected semi-axis in the galactocentric direction
E_{mea}	measured cavity energy, considered the cavity's enthalpy H
E_{inj}	injected energy
P_{jet}, P'_{jet}	intrinsic and projected cavity jet power
\overline{P}_{jet}	cumulative jet power
\widetilde{P}_{jet}	time-averaged cycle-corrected jet power
ΔP_{jet}^{rel}	relative jet power change

Introduction

Active galactic nuclei (AGN) feedback plays a crucial role in the evolution of systems harbouring hot atmospheres – such as giant ellipticals (gE), galaxy groups (GGr) and galaxy clusters (GC). It has been shown many times that AGN feedback prevents gas in the centre of the hot atmospheres from cooling at the rates predicted by the models of cooling flows resulting from radiative cooling. Instead, surface brightness depressions, known as X-ray cavities, have been observed in nearly all cool-core (CC) systems.

X-ray cavities are a key observational sign of radio-mechanical AGN feedback. When the supermassive black hole (SMBH) at the centre of a hot atmosphere accretes at low accretion rates, it is likely to form jets. The jets then excavate the cavities, which, after detaching, continue to rise buoyantly through the atmosphere until they fade away from our view. Although the precise mechanism of energy dissipation is far from being constrained, it is known that the presence of X-ray cavities heats the surrounding gas.

X-ray cavities provide an opportunity to quantify the AGN feedback cycle. Their morphology and distance from the centre determine the energy input from the SMBH, and – together with the age estimates – we can then calculate the mechanical power of the jet that formed the cavity. By investigating systems with multiple episodes of AGN feedback, i.e., multiple generations of cavities, we aim to put constraints on the jet power non-variability.

Chapter 1 introduces hot atmospheres in general. We look at the origin of X-ray emission, present the cooling flow problem and the paradigm shift it has undergone. Discussion on the nature of cold gas content found in giant ellipticals concludes the first chapter.

A closer look at AGN feedback effect, its manifestations and characteristics opens up Chapter 2. Focusing on radio-mechanical AGN feedback, X-ray cavities are introduced after, and their energetics and timescales are mentioned in greater detail. The chapter concludes with various scenarios that potentially explain the misalignments found in some multiple-cavity systems.

Chapter 3 presents our target sources and summarises data analysis carried out to investigate cavity jet powers, inclination effects and the possibility of precession in misaligned systems. Our approach to spectral and image analysis is laid out. We also outline an alternative approach to calculating cavity ages and energy that was adopted.

Our results are presented in Chapter 4 and further discussed in Chapter 5. Each galaxy is examined individually. We focus on the jet power estimates as a result of our improved calculation methodology. In the latter parts of both chapters, we turn to a toy model as a simplification to study the projection effects on measured jet powers.

Chapter 1

Hot atmospheres

Hot atmospheres are a common term to describe hot X-ray emitting plasma filling the space between individual galaxies in galaxy clusters and enveloping early-type galaxies.

The presence of hot atmospheres around galaxy clusters was discovered by the first X-ray telescope *Uhuru*, launched in 1971. *Uhuru* detected extended emission around already known X-ray point sources in the Coma cluster (Gursky et al., 1971) and the Perseus cluster (Forman et al., 1972). Extended emission was then identified as bremsstrahlung of thermal origin from the hot X-ray emitting gas enveloping the cluster galaxies. *Einstein Observatory* later confirmed these observations and identified hot atmospheres around individual galaxies, e.g., around M87 (Schreier et al., 1982) and other ellipticals in the Virgo cluster (Forman et al., 1979). *ROSAT* then attested to the previous detections of hot atmospheres, and *Chandra X-ray Observatory's* and *XMM-Newton's* higher spatial resolution revealed intricate details and disturbances of the atmospheres.

The masses of such atmospheres range between $10^{14} - 10^{15} M_{\odot}$ in galaxy clusters and $10^{13} - 10^{14} M_{\odot}$ in giant ellipticals (Forman et al., 1985). The typical temperature of the hot gas is about $\sim 10^6$ K in gEs, increasing to $\sim 2 \cdot 10^7$ K and higher in GCs. In good approximation, the atmosphere as a whole can be considered to be in hydrostatic equilibrium.

The existence of hot atmospheres around galaxy clusters, galaxy groups (GGr) and around early-type galaxies is linked to the hierarchical structure formation in the Universe. In the framework of the Λ -CDM model, the baryonic matter fell into gravitational potential wells of dark matter halos. During the infall, the baryonic gas was shock-heated to the temperatures of $10^7 - 10^8$ K and continued to accrete onto the central regions. The heated accreted gas formed the first X-ray atmospheres of the “red nuggets”, early-type galaxies’ predecessors observed at redshift $z \geq 2$ (Werner et al., 2019). Red nuggets then grew by accretion and mergers into the present-day ellipticals.

Although we focus on giant ellipticals, their atmospheres differ only marginally from those in galaxy clusters due to the self-similarity of the mentioned systems, allowing us to describe the properties of hot atmospheres universally.

Giant elliptical galaxies represent early-type galaxies of the Hubble sequence. Nearly all of them harbour hot atmospheres, whose origin can be traced to the early universe’s structure formation. In comparison to normal ellipticals, they are more massive and, therefore, more luminous. They also rotate more slowly due to the dry mergers they

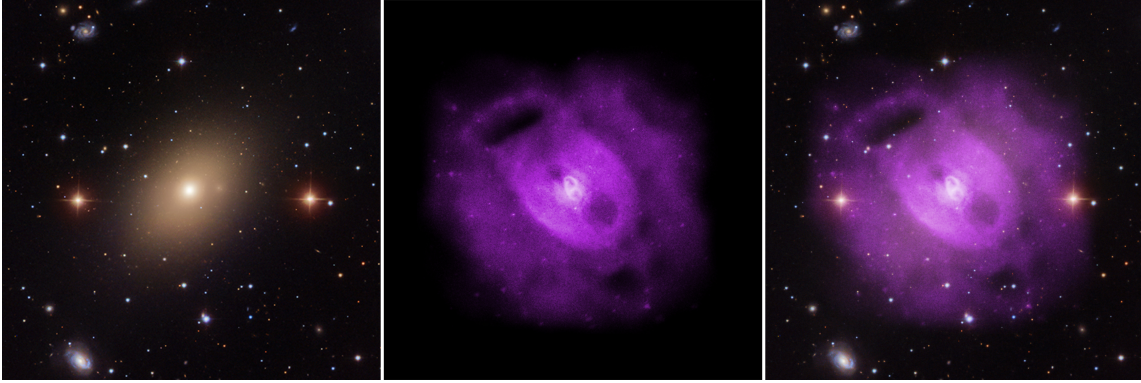


Figure 1.1: Giant elliptical galaxy NGC 5813 in the Virgo constellation. Left: optical. Centre: X-ray. Right: composite. Author: X-ray: NASA/CXC/SAO/S.Randall et al., Optical: SDSS.

underwent, during which they lost angular momentum. Their isophotes, i.e., the lines along which surface brightness is constant, tend to be boxy. The optical brightness profile of the outer regions is well described by a Sérsic profile, but the trend flattens toward the centre. One of the possible explanations is a SMBH ejecting the stars from the central regions, therefore reducing the emission of optical-wavelength light in the core.

1.1 X-ray emission

Hot atmospheres are essentially dilute optically thin X-ray emitting plasma of collisionally ionised gas in ionisation equilibrium with temperatures of $\sim 10^7 - 10^8$ K (McNamara and Nulsen, 2007). The temperature typically increases outwards (Mathews and Brighenti, 2003). Generally, number density of hot atmospheres decreases outwardly from $\sim 10^{-1} \text{ cm}^{-3}$ in the centre to $\sim 10^{-4} \text{ cm}^{-3}$ at larger radii. Following deprojected semi-analytical β -model (Cavaliere and Fusco-Femiano, 1976), the gas density profile can be approximated as

$$n_{\text{gas}}(r) = n_{\text{gas}}(0) \left[1 + \left(\frac{r}{r_c} \right)^2 \right]^{-3\beta/2}, \quad (1.1)$$

where $n_{\text{gas}}(0)$ is the central density value, r_c is the core radius, r is the radial distance from the centre and β typically has a value of $\sim 0.3 - 0.5$ for gEs.

Since the hot gas is composed of free electrons and atomic nuclei, the electrons are continuously decelerated in the nuclei' Coulomb fields and thus emit radiation in the form of photons. This two-body emission process is known as thermal bremsstrahlung (or free-free emission) and is the source of a continuum in an X-ray spectrum. Bremsstrahlung emissivity ϵ of the fully ionised plasma is proportional to the square of the number density of particles n , $\epsilon \propto n^2$.

X-ray spectral continuum is interwoven with line emission of heavier elements, such as iron, sulphur, silicon, magnesium, oxygen and carbon. Line emission origi-

nates in the radiative de-excitation of collisionally excited plasma. Due to the excitation's two-body nature, this process also scales with n^2 . The strength of the emission line is given by the abundance of the given metal and the nuclear charge of its ion, causing some of the strongest lines to be those of iron. The presence or absence of certain emission lines and the relative strengths of the emission lines depend heavily on the temperature of the plasma. Therefore, analysis of the X-ray spectrum can reveal the presence of mechanisms like radiative cooling in galactic atmospheres. For example, Fe XVII lines are indicators of 0.5 keV gas and O VII of the gas with a temperature of 0.2 keV.

1.2 Cooling flows

X-ray emission from thermal bremsstrahlung and the line emission causes the gas to cool radiatively at a cooling rate C , which can be thought of as the energy loss per unit volume and unit time. Cooling rate C is proportional to the square of the number density, and the cooling function Λ is then defined as the proportionality factor between the two:

$$\Lambda(T) := \frac{C}{n^2}. \quad (1.2)$$

Based on [Schneider \(2006\)](#), the cooling time t_{cool} , i.e., the time it would take the gas to lose all of its energy at a constant cooling rate – can be calculated as

$$t_{\text{cool}} = \frac{3nkT}{2C} = \frac{3kT}{2n\Lambda(T)}. \quad (1.3)$$

If the cooling time t_{cool} is longer than the age of the system¹, the gas remains more or less isothermal. On the other hand, if the cooling time is shorter than the age of the system, the gas effectively begins to cool. Since $t_{\text{cool}} \propto n^{-1}$, the satisfactory cooling time can be achieved only in the densest regions of the atmospheres – at their centres.

As the gas starts to cool, hydrostatic equilibrium can no longer be sustained as the gas pressure decreases unless the overlying gas flows inward and compresses the gas ([Fabian, 1994](#)). Increasing the density would then further shorten t_{cool} , r_{cool} would extend, and surface brightness would be strongly peaked at the centre of the system. Single-phase isobaric models also predict the presence of prominent Fe L shell transition lines together with O VIII lines ([Peterson and Fabian, 2006](#)). If radiative cooling time is longer than or nearly equal to dynamical and sound-crossing time, then such a flow is highly subsonic and maintains hydrostatic equilibrium ([Mathews and Brighenti, 2003](#)). The rate of the inward-flow is calculated as mass cooling rate according to

$$\dot{M} \sim \frac{2\mu m_p}{5kT}. \quad (1.4)$$

It can be easily shown that for $T \sim 10^8$ K and typical X-ray luminosities ranging from 10^{40} to 10^{43} erg/s, the expected mass cooling rate lies between $0.005 - 5 M_{\odot}/\text{yr}$.

¹Often $t_{\text{age}} = H_0^{-1}$ is considered.

CC clusters are characterised by a lower entropy profile, significantly shorter central cooling time, and a systematic temperature drop at the centre compared to NCC clusters (Hudson et al., 2010). Numerical simulations by Burns et al. (2008) suggest that NCC clusters form through mergers of CC clusters, with the merger process disrupting the cooling core and subsequent gas mixing preventing its re-establishment. This suggests that rather than being two strictly distinct subclasses, NCC and CC clusters may represent different evolutionary stages in the formation history of galaxy clusters.

Overall, the absence of line emission that would indicate the presence of cooling gas (< 0.2 keV), combined with short central cooling times and the “red-and-dead” nature of the studied systems, suggests the need for a mechanism that can plausibly account for these observations. The most compelling explanation appears to be heating by AGN feedback.

1.3 Cold gas

A resonant study of a few nearby gEs was done by Werner et al. (2014), which showed that a cold gas tracer [C II] was detected in all galaxies with H- α + [N II] nebular emission, proving that gEs could contain large reservoirs of cold gas. Both types of emission originate in the same place, together with low-entropy soft X-ray plasma. Moreover, Werner et al. (2014) showed that cool-gas-rich galaxies are more prone to thermal instabilities, hinting at the possibility of cold gas being produced by cooling from hot plasma. This view is also supported by the fact that systems with extended nebular emission have lower entropies outside the innermost regions than cool-gas-poor systems (e.g., Werner et al., 2014; O’Sullivan et al., 2018; Lakhchaura et al., 2018).

Presence of another cold gas tracer, molecular CO, was investigated by O’Sullivan et al. (2018) in early-type galaxies in nearby galaxy groups (within 80 Mpc). Cold gas, either in the form of atomic H I gas or molecular CO gas, was found in at least half of the targeted systems. Molecular gas usually amounted to about $10^7 M_{\odot}$ while H I masses fell within the range $10^6 - 10^{10} M_{\odot}$. Cold gas was usually found in discs and was acquired either by interactions with neighbouring galaxies or by condensation from the hot phase, as suggested in Werner et al. (2014).

Lakhchaura et al. (2018) found that around half of the studied giant ellipticals have notable H- α + [N II] emission in the form of filaments. There does not seem to be a link between the presence of H- α + [N II] emission and general properties of gEs like X-ray luminosity L_X or total gas mass M_{gas} , however a weak positive correlation between jet power P_{jet} and luminosity of H- α + [N II] $L_{\text{H-}\alpha\text{+[N II]}}$ which could have substantial aftermath on the accretion mode of the SMBH (Lakhchaura et al., 2018). Furthermore, Lakhchaura et al. (2018) found that H- α + [N II] emission seems to be present in the galaxies with shorter cooling times and more disturbed X-ray morphology.

According to Werner et al. (2019), the origin of such complex emission spanning across at least 6 orders of magnitude in temperature lies in the structure of the filamentary cool gas. Strands of CO and [C II]-emitting gas at ~ 1000 K are enveloped by H- α + [N II] and UV emitting phase and embedded into soft-X-ray-emitting gas that is cooler than the surrounding atmosphere. The mechanism is illustrated in Fig. 1.3.

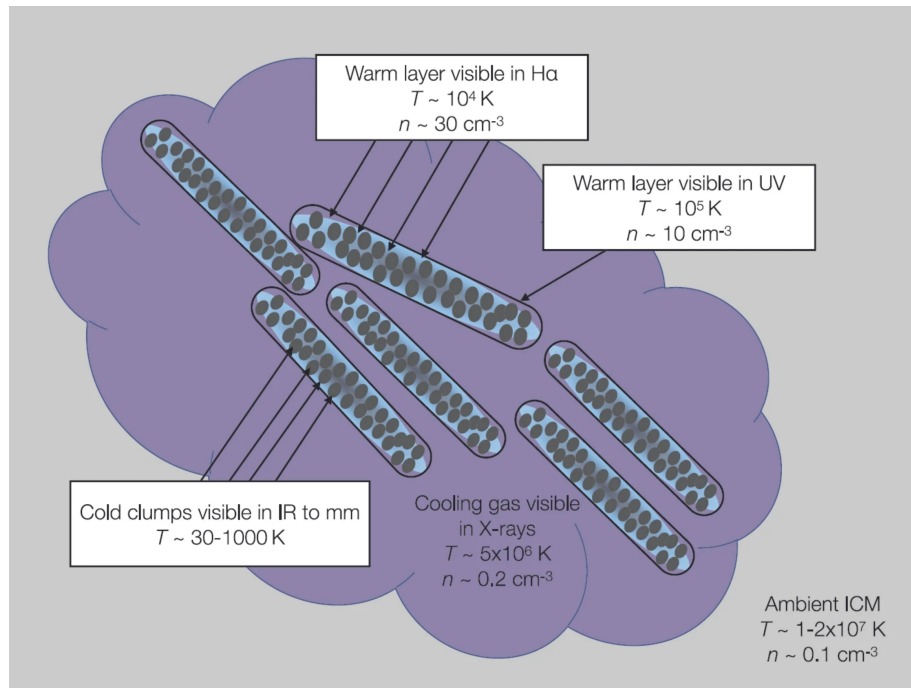


Figure 1.3: Multiphase gas emission in hot atmospheres. From Werner et al. (2019) (based on Werner et al., 2013; Anderson and Sunyaev, 2018).

Table 1.1: Multiphase gas components in ellipticals, based on Lakhchaura et al. (2018) and referenced therein.

Temperature	Element/molecule	Process/occurrence	Observing band
$\lesssim 30$ K	CO	molecular clouds	radio
~ 100 K	[C II], [N II], [O I]	cooling lines	far infrared
~ 1000 K	H ₂	molecular clouds	near infrared
$\sim 10^4$ K	H- α + [N II]	ionized nebular emission	optical
$\sim 10^5$ K	C IV, He II	line emission	UV ¹
$\sim 10^7$ K		thermal bremsstrahlung, line emission	X-ray

¹ Sparks et al. (2012)

Chapter 2

AGN feedback & X-ray cavities

2.1 AGN feedback

It is a truth universally acknowledged that active galactic nuclei possess SMBHs at their cores, which need cold gas to fuel their energy production. The infalling matter forms an accretion disc to reduce its angular momentum. There, the gas undergoes friction and momentum transfer, thus heating the gas, which then radiates away its excess energy. The interaction of the emitted energy and the surrounding gas leads to the AGN feedback process, operating as a self-regulating cycle.

AGN feedback operates in two distinctive modes depending on the SMBH's accretion rate. First, in the case of a high accretion rate, *the quasar / kinetic* AGN feedback mode ensues. Radiatively efficient optically thick but geometrically thin accretion disc heats the surrounding gas and can even change the ionisation of the gas, which then alters the cooling curve of the gas (Schneider, 2006; Hlavacek-Larrondo et al., 2022).

Secondly, *radio / radio-mechanical* mode AGN feedback sets in when the SMBH accretes at much lower rates than the Eddington rate. The accretion disc is optically thin and, therefore, radiatively inefficient, causing inward energy advection, which can propel jets (Narayan and Yi, 1994). The jets then inject mechanical energy into the surrounding gas, which leads to the formation of bubbles devoid of X-ray emission, which are now commonly referred to as X-ray cavities (Schneider, 2006). This seems to be the case for most of the AGNs in clusters and groups, but radio-mechanical AGN feedback is predominantly manifested in cool-core systems (Dong et al., 2010; Fabian, 2012; Shin et al., 2016).

Ultimately, the interaction between the SMBH and the surrounding gas leads to either an increase in the atmosphere temperature or gas displacement. The gas then flows inwards, fuels the SMBH in the centre and thereby triggers yet another episodic activity of AGN. A vicious self-regulating feedback loop is created.

The self-regulatory nature of such a feedback loop, in which heating and cooling rates are coupled, can be explained by the following counter-argument: if the cooling and heating rates were not tied, the heating rate would not only match but soon exceed the cooling rate resulting in the net heating of the atmospheres which would cause cooling times to be comparable to Hubble times which is contrary to the observations (McNamara and Nulsen, 2007).

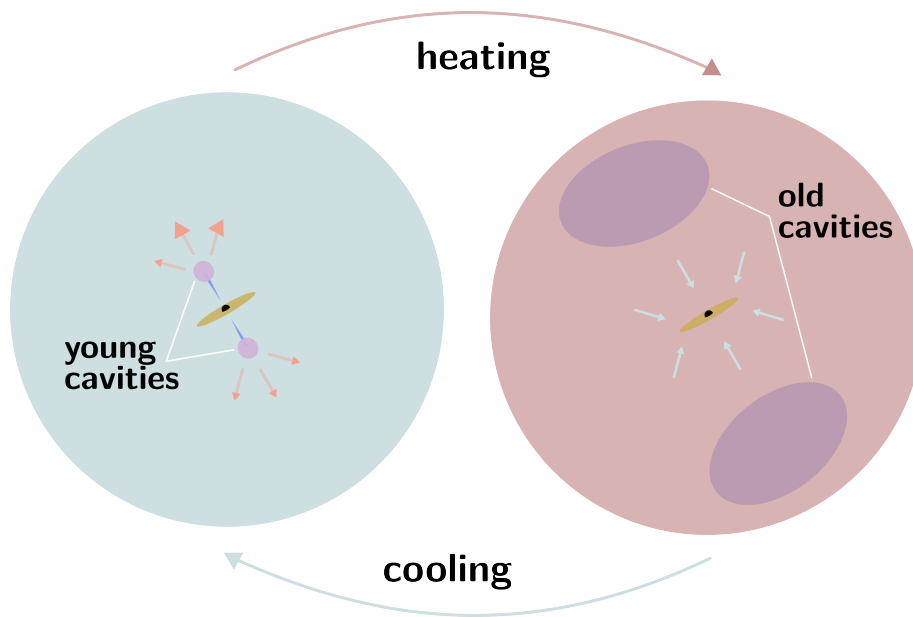


Figure 2.1: Sketch of radio-mechanical AGN feedback.

Not long after *Chandra* and *XMM-Newton* revealed discrepancies between the theoretical models of cooling flows and the observational evidence of the lack of their supposed strength, an idea of radio-mechanical AGN feedback delaying massive cooling was proposed. This idea has been proven to be convenient, as illustrated, for example, in Fig. 2 in [Bîrzan et al. \(2004\)](#) or in Fig. 6 in [Rafferty et al. \(2006\)](#).

Mechanical power of the AGN jets is closely tied to the accretion mode of the SMBH. [Allen et al. \(2006\)](#) found a power-law correlation between Bondi accretion rate and jet powers. While hydrodynamic equations can be worked out analytically ([Bondi, 1952](#)), the Bondi accretion is not physically viable since the model assumes adiabaticity, spherical symmetry and disregards angular momentum, which is usually non-zero for infalling matter. [Plšek et al. \(2022\)](#) found that the correlation between Bondi accretion power and jet power is more significant in galaxies with reported $H\text{-}\alpha + [\text{N II}]$ emission, which are likely to host thermally unstable atmospheres.

On the other hand, the chaotic cold accretion (CCA) model has also been proposed as a plausible accretion mechanism. [Pizzolato and Soker \(2005\)](#) proposed a generalised CCA model where hot, over-dense gas blobs lose energy faster than the surrounding medium. As they sink toward the centre, the drag force strips them of their angular momentum, and SMBH can easily accrete such overdensities. According to [Gaspari et al. \(2013\)](#), CCA can drive the AGN feedback in various systems. In this scenario, the response of the SMBH to the infalling matter is quicker, which then makes the whole feedback cycle more efficient.

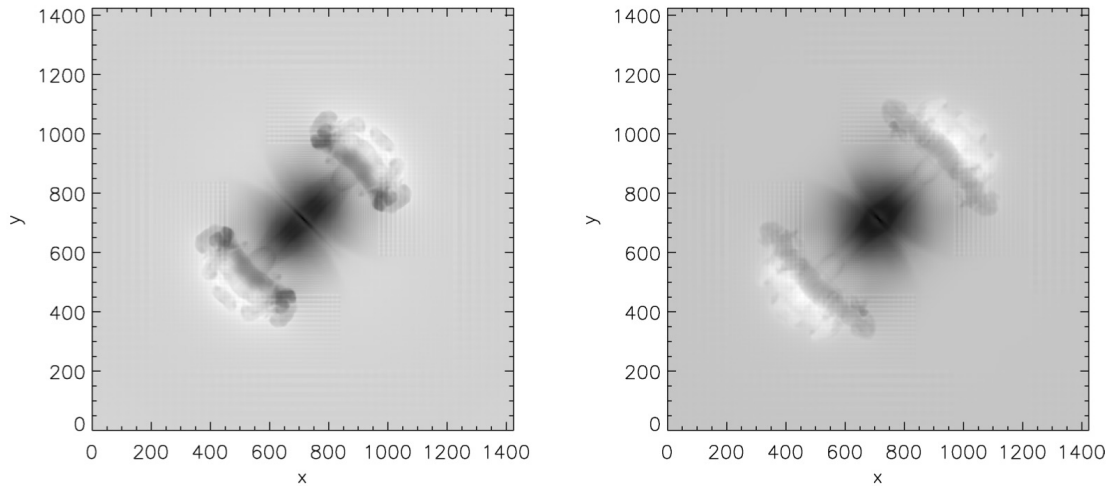


Figure 2.2: Synthetic *Chandra* X-ray flux images of cavities resulting from simulations with subgrid turbulence. The left panel shows the cavity 155 million years after it was launched, the right 205 million years after. Taken from Brüggen et al. (2009).

2.2 X-ray cavities

X-ray cavities are regions of diminished line-of-sight X-ray emission within the hot atmospheres. They are associated with central AGN activity and are key indicators of the sustained radio-mechanical AGN feedback. Disturbances of hot atmospheres were first observed by the Einstein observatory in the NGC 1275 / Perseus cluster (Fabian et al., 1981). Boehringer et al. (1993) deduced that the known disturbances in the NGC 1275 were indeed regions devoid of X-ray emission and additionally found that radio emission coincided with the cavities. Subsequent *Chandra's* and *XMM-Newton's* observations shed more light on their origin, nature and energetics.

X-ray cavities are most commonly thought to be low-density ellipsoidal bubbles filled with relativistic plasma that are in pressure equilibrium with the surrounding gas (e.g., Churazov et al., 2002; Bîrzan et al., 2004). They are often spatially co-aligned with synchrotron radio emission (*radio lobes*), but the radio emission tends to fade more quickly. The older cavities without radio emission are then dubbed "ghost" cavities.

The cavity origin lies in the jet-ICM interaction. Due to the radiatively inefficient accretion flow, AGN launches a pair of bipolar jets (e.g., Churazov et al., 2002; Hlavacek-Larrondo et al., 2022). The jets then inflate a small underdense bubble. In its early evolutionary stages, the cavity expands slightly supersonically. Such processes can drive weak shocks, which can heat the gas in the centres of atmospheres (Mathews et al., 2006). During later stages of cavity evolution, buoyancy takes over the bubble's rise through the atmosphere and the cavity expands adiabatically (Churazov et al., 2002; Hlavacek-Larrondo et al., 2022).

X-ray cavities are observed as elliptical or circular regions, but their true shapes are more intricate. Simulations have shown that their intrinsic shape more or less resembles an atomic mushroom cloud (e.g., Brüggen et al., 2009; Guo, 2015). Usually, they are approximated to be either oblate or prolate spheroids. Guo (2020) showed that during

the buoyancy stage of the bubble's life, it tends to become more elongated in the direction perpendicular to the direction towards the galactic centre, i.e., the galactocentric direction.

Many studies have found that X-ray cavities are more likely to form in cool-core systems. [Fabian \(2012\)](#) found that nearly every nearby CC cluster harbours X-ray cavities. [Dong et al. \(2010\)](#) investigated the incidence of X-ray cavities in galaxy groups and found that potentially, half of the sample showed signs of regions devoid of X-ray emission, and every one of them was a CC system.

2.2.1 Cavity timescales

Estimating the age of the cavity depends significantly on the interpretation of its origin. Firstly, if we suppose that the cavity is created by a high-momentum AGN jet, then the age can be calculated as the time it takes for the cavity to rise to its projected distance at a constant velocity. The presence of weak shocks around the innermost cavities indicates that the expansion speed can be slightly supersonic (e.g., [McNamara and Nulsen, 2007](#); [Fabian, 2012](#)). Thus, sound speed, given by

$$c_s = \sqrt{\frac{\gamma k T}{\mu m_H}}, \quad (2.1)$$

where γ is an adiabatic index of the surrounding gas, μ is the mean molecular weight and m_H is the mass of a hydrogen atom, becomes relevant expansion velocity for such a cavity. The age of such a cavity is then given by

$$t_{ss} = \frac{d}{c_s}. \quad (2.2)$$

Secondly, if we consider that the cavity rises purely buoyantly from the galaxy centre to its projected distance, then its terminal velocity can be approximated as

$$v_{buo} \sim \sqrt{\frac{2gV}{SC}}, \quad (2.3)$$

where V is the volume of the cavity, S is the cross-section of the cavity and C is the drag coefficient. The buoyancy timescale is calculated as

$$t_{buo} = \frac{d}{v_{buo}}. \quad (2.4)$$

Cavity ages are typically in the order of $\sim 10^6$ up to $\sim 10^8$ years, indicating their long-lived stability. Contrary to observations, Rayleigh-Taylor instabilities could, in principle, develop and shred the cavity ([McNamara and Nulsen, 2007](#)). Their formation can be suppressed, if we assume the quasi-continuous injection or magnetically dominant bubbles (e.g., [Diehl et al., 2008](#); [Brüggen et al., 2009](#)).

2.2.2 Cavity energetics

Measuring the energy deposited into the cavities can help us quantify the feedback cycle of SMBHs. Jet powers are usually calculated as

$$P_{\text{jet}} = \frac{H}{t}, \quad (2.5)$$

where H denotes the enthalpy of a cavity and t its age (e.g., [Bîrzan et al., 2004](#); [Diehl et al., 2008](#); [McNamara and Nulsen, 2007](#); [Guo, 2020](#)). Enthalpy is usually estimated by

$$H = \frac{\gamma}{\gamma - 1} pV, \quad (2.6)$$

where γ is the ratio of specific heats, p the pressure of the ambient medium at the cavity distance d and V the cavity volume. [McNamara and Nulsen \(2007\)](#) notes that Eq. 2.6 holds if the cavity is filled with ideal gas whose ratio of specific heats γ is constant. In any case, enthalpy ranges between $2pV$ if the bubble is dominated by the magnetic fields and $4pV$ for the bubble filled with relativistic particles. In giant ellipticals, pV amounts to about $\sim 10^{55}$ erg and in galaxy clusters it reaches about $\sim 10^{61}$ erg. ([McNamara and Nulsen, 2007](#)).

According to [Bîrzan et al. \(2004\)](#), the cavity's rise through the atmosphere is powered by the release of potential energy of the gas falling inward at the vacant region where the cavity was. The energy is then transformed into heat with an efficiency approaching one. However, substantial energy can be deposited into shocks and a small part carried away by sound waves ([Churazov et al., 2002](#); [McNamara and Nulsen, 2007](#)).

Mechanical energy exchanged between the cavity and the surrounding gas can, under the assumption of adiabatic expansion and the pressure equilibrium with the surrounding gas, be expressed as

$$\Delta E = - \int V \rho \frac{d\Phi}{dr} = - \int V dp = E_0 \left[1 - \left(\frac{p}{p_0} \right)^{1-1/\gamma} \right], \quad (2.7)$$

where E_0 is the initial energy of the cavity, p the pressure at its current projected distance and p_0 the pressure ([Churazov et al., 2002](#)).

2.3 Misalignments in multi-cavity systems

Systems with multiple generations of X-ray cavities not only provide critical information about the duty cycle of SMBH but also reveal the peculiarities of jet-ICM interactions. It is not yet clear why some systems are strongly aligned (e.g., NGC 5813, see Fig. 1.1) compared to the ones that showcase significant alignment deviations between individual generations.

[Ubertosi et al. \(2024\)](#) combined VLBA and *Chandra* data to investigate the possible sources of misalignment between currently-active jets and X-ray cavities in various cool-core galaxy clusters and groups, both aligned and misaligned. The study found that projection could affect possible misalignments in about one-third of the cases.

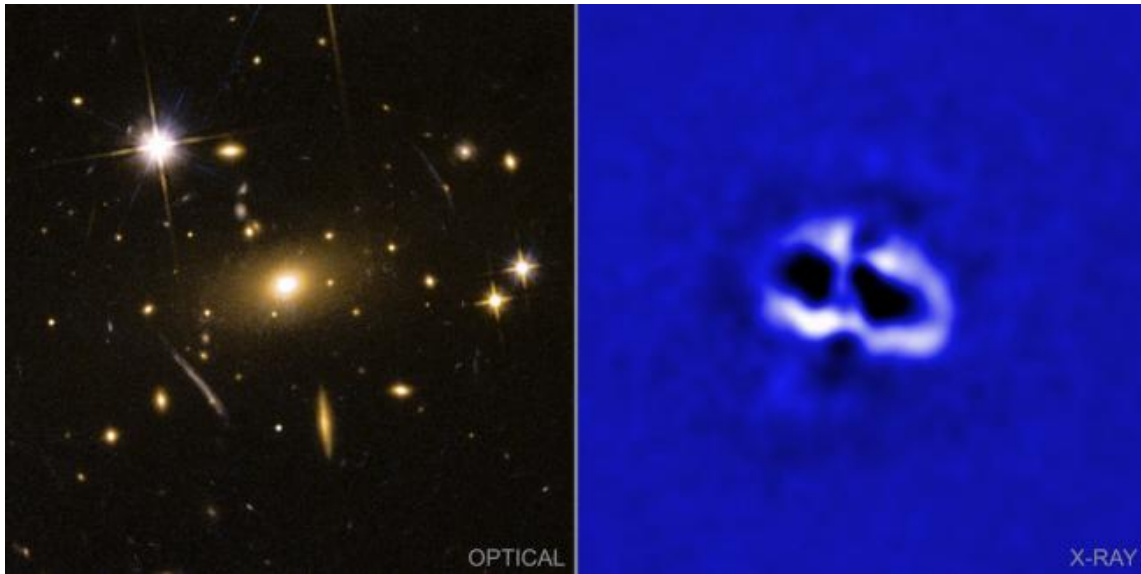


Figure 2.3: Galaxy cluster RBS 797 with two equidistant cavity pairs perpendicular to each other. Author: NASA / CXC / University of Bologna / F. Ubertosi / STScI / M. Calzadilla / NSF / NRAO / ALMA.

All targets but one showed signs of sloshing. However, even if the bulk gas motion can affect the cavity position, it cannot be the primary source of misalignment.

If jet reorientation is responsible for the observed misalignments, then it is more likely to cause misalignments larger than 45° . Jet reorientation events could explain some orthogonal placements of cavities. On the other hand, the question of which jet reorientation event can be physically possible to create such misalignment is far from easy to answer.

One of the possible explanations for a jet changing its orientation can be its precession. However, it has been shown that precession is likely to happen at shorter timescales than the observed age difference between cavity ages (e. g. [Schellenberger et al., 2021](#); [Britzen et al., 2018](#); [Ubertosi et al., 2021](#)). One could argue that the possibility of a jet suddenly turning off and back on in a single precession period is not plausible. On the other hand, there is no need for jet switching off/on if we consider that it is the bubble that can detach irrespective of the jet.

Reorientation can also be explained by changes in the accretion rates or in the geometry of the accretion disc of the central AGN engine. For example, the randomness of the directions of infalling clouds in CCA can change the angular momentum of the central AGN. By aligning the direction of angular momentum of the SMBH with the jet direction, a change in the SMBH's momentum leads to jet reorientation and, consequently, a change in the positional angle of a future cavity. It seems that a binary black hole could potentially drive simultaneous cavity formation. This seems to be the case in the galaxy cluster RBS 797 ([Ubertosi et al., 2021](#)), where the cavity generations are perpendicular to each other and their distance from the centre, together with their ages, are nearly the same.

Chapter 3

Data analysis

Archival data from *Chandra X-ray Observatory* were downloaded for targets summarised in Tab. 3.1. All available non-grating ACIS-S and ACIS-I observations for each source were reprocessed through *chandra_repro* script (*CIAO 4.17*, Fruscione et al., 2006) and reprojected. Point sources were identified by the *wavdetect* algorithm. Background light curves for each observation were extracted. The *deflare* routine was applied to every observation to remove the intervals with higher background counts caused by soft proton contamination or interaction of energetic particles of the cosmic background.

Table 3.1: Studied giant elliptical galaxies.

	NGC 5813	NGC 5044	NGC 4649	NGC 4472
α [h:m:s]	15:01:11.37	13:15:23.97	12:43:40.00	12:29:46.80
δ [d:m:s]	1:42:05.86	-16:23:07.12	11:33:09.53	8:00:02.51
D [Mpc]	31.012 ± 2.052	38.013 ± 2.187	16.702 ± 0.449	16.060 ± 0.348
z	0.006525	0.009280	0.003703	0.000023
σ [km/s]	236.0 ± 3.4	224.9 ± 9.1	330.5 ± 4.6	282.0 ± 2.9
Scale [kpc/'']	0.153	0.219	0.102	0.0938
n_{H} [10^{20} cm^{-3}]	5.2	6.36	2.3	1.64
M_{\bullet} [$10^8 M_{\odot}$]	7.1^1	2.1^2	44.4^1	25.4^3

¹ Saglia et al. (2016)

² Schellenberger et al. (2021)

³ Kormendy and Ho (2013)

3.1 Spectral analysis

In preparation for spectral extraction, background event files were created for each reprojected event file from the *CALDB 4.12.0* database via the *blanksky* command. The *specextract* routine was used to extract spectra from each reprojected event file, with the point sources left out. Spectra were extracted from a set of concentric annuli centred

at the X-ray emission peak¹ from each reprojected observation, and subsequently, individual spectral files were combined for each annulus with the *combine_spectra* command.

Spectral analysis was carried out via *PyXspec 2.1.4* module (*Xspec 12.14.1*, Arnaud, 1996). Every combined spectrum was fitted with a model that accounted for the deprojection (*projct* component), the line-of-sight photoelectric absorption due to the atomic and molecular hydrogen in our Galaxy (*phabs* component), the bremsstrahlung emission of Low-mass X-ray binaries (*bremss* component) and the emission of collisionally-ionised plasma in equilibrium (*apec* component). The resulting 11-parameter model we used was

$$m = \text{projct}*(\text{phabs}*(\text{apec})) + \text{phabs}*(\text{bremss})^2.$$

The cosmology was set to be $H_0 = 70$ km/s/Mpc, $q_0 = 0$, and $\Lambda_0 = 0.7326$. The *Cash* statistics and the *Levenberg-Marquardt* algorithm was used for spectral fitting. Photoelectric absorption cross-sections were taken from Balucinska-Church and McCammon (1992). Abundances for *apec* component's *Abundanc* parameter were expressed relatively to abundance tables taken from Lodders et al. (2009). To account for the absorption of low-energy X-ray photons caused by our Galaxy, the hydrogen column density N_{H} (*nH* parameter in *phabs* component) was set to the values taken from the *nHtot* tool³. In some cases, if the Galactic absorption turned out to be higher than the provided value, N_{H} was also fitted.

The spectral analysis aimed to produce deprojected radial profiles of temperature and electron density. The temperature (kT) profile was extracted from the *apec* component. Electron density n_e profile was determined from *apec norm N* parameter which is given for every annulus as

$$N = \frac{10^{-14}}{4\pi D^2} \int n_e n_{\text{H}} dV, \quad (3.1)$$

where D is the distance of the source⁴, n_{H} is the hydrogen density and dV is the element volume. Assuming n_e to be constant in the given annulus and corresponding to approximately $1.2n_{\text{H}}$, the integrated volume element becomes the volume of the shell with radii corresponding to those of the annular region.

A Markov chain Monte Carlo algorithm was used to derive the parameter estimates and their uncertainties. The median of the chain was adopted as the best-fit value. The uncertainties were taken as an equivalent to 1σ confidence interval at 16% and 84% quantiles.

¹Given by a centroid in *DS9*.

²The second appearance of *phabs* component arises from the fact that while the *bremss* component does not require deprojection, it is still subject to the same amount of photoelectric absorption as the *apec* component.

³<https://www.swift.ac.uk/analysis/nhtot/>, based on Willingale et al. (2013).

⁴We used redshift-independent measurements from NED database.

3.2 Image analysis

For image analysis, we added up the observations into the exposure-corrected images across the *soft* (0.5 – 1.2 keV), *medium* (1.2 – 2 keV), *hard* (2.0 – 7.0 keV) and *broad* (0.5 – 7 keV) energy range using the `flux_obs` command. For each image, left-out point sources were filled through `dmfilth` with background Poisson noise extracted from annular regions extending just slightly beyond the point sources.

Resulting broad or soft band images were fitted with the β -model. Assuming hydrostatic equilibrium and isothermality, the projected surface brightness profile can be determined by β -model that takes the form of

$$S(b) = n_0^2 r_c \Lambda(T_{\text{gas}}) B(3\beta - 0.5, 0.5) \left[1 + \left(\frac{b}{r_c} \right)^2 \right]^{0.5-3\beta}, \quad (3.2)$$

where n_0 is the central density, r_c the core radius, $\Lambda(T_{\text{gas}})$ the cooling function of the gas at the temperature T_{gas} , $B(3\beta - 0.5, 0.5)$ the beta function and b is the projected distance. β parameter describes the steepness of the whole surface brightness profile (Ettori, 2000).

Subtracting the model from the image revealed regions of suppressed X-ray emission, which were identified as individual cavities. They were estimated by hand in DS9 as ellipse regions. Each cavity is described by five parameters: right ascension α and declination δ of the centre of the ellipse, two semi-axis R_x , R_y and rotation angle A^5 .

A simple routine was developed to find the cavity distance d , the axis closest to the supposed direction to the galactic centre R_l , and the axis perpendicular to the galactocentric direction R_w . To infer the physical sizes of d , R_l and R_w , cosmology-corrected scale from NASA/IPAC Extragalactic Database (NED)⁶ was used.

We also adjusted the angles so that the cavity direction within the system is well described by the cavity positional angle φ_{pos} measured from the x -axis towards the semi-major cavity axis and the cavity rotation angle φ_{rot} measured from the semimajor cavity axis towards the galactocentric direction. The angles are depicted in Fig. 3.1.

From inferred axis sizes, the cavity volume V was calculated as

$$V = \frac{4}{3} R_l R_w^2 \quad (3.3)$$

and the cross-section S as

$$S = \pi R_w^2. \quad (3.4)$$

Alternatively, the machine-learning pipeline CADET (Plšek et al., 2023) was employed for cavity identification. Its convolutional neural network detected potential cavities in the re-binned input images, which were subsequently broken down into individual cavities. For these decomposed cavities, their volumes, cross-sections, and rotational angles were automatically estimated by the CADET pipeline.

⁵Measured from the x -axis anti-clockwise towards the axis closest to the x -axis before rotation.

⁶ $H_0 = 67.8 \text{ km/s/Mpc}$, $\Omega_{\text{matter}} = 0.308$, $\Omega_{\text{vacuum}} = 0.692$

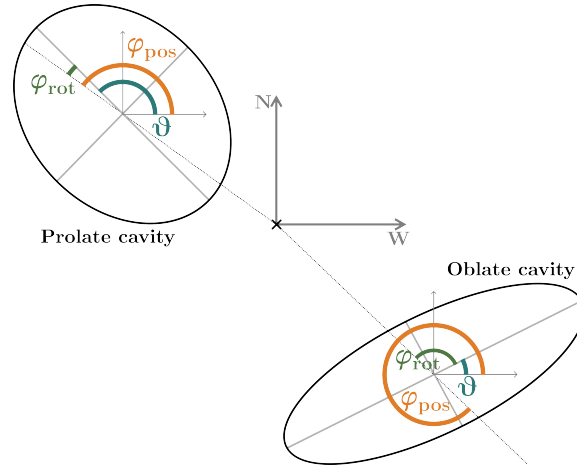


Figure 3.1: Cavity angles describing the cavity's position within the system.

3.3 Timescales

Timescales of X-ray cavities were calculated according to Sect. 2.2.1. The value of kT at the cavity distance d was linearly interpolated from the nearest values. For the sound-speed timescale (Eq. 2.1 and Eq. 2.2), the ratio of specific heat γ of the atmosphere was considered to be $\gamma = 5/3$ and the mean molecular weight $\mu = 0.62$.

When it came to the buoyancy timescale (Eq. 2.3 and Eq. 2.4), we considered $C \approx 0.75$ (Churazov et al., 2002; McNamara and Nulsen, 2007). Assuming a galaxy as an isothermal sphere allowed us to approximate g as

$$g \approx 2\sigma^2/d, \quad (3.5)$$

where the stellar velocity dispersion σ was taken from *HyperLEDA* database⁷ (Makarov et al., 2014).

3.3.1 Timescale correction

In our approach, we considered the innermost cavity generation (also referred to as *the first generation*) to be still attached to the jet excavating it. Such a cavity should expand mildly supersonically. Using the sound-speed timescale, therefore, provides an upper limit for the age of an attached cavity.

For *the second generation*, we considered the bubble to be driven purely by buoyancy. The buoyancy timescale corrected by the sound-speed timescale of the previous generation was thought to best approximate the cavity age of the second generation. The correction was done based on the fact that the buoyancy force can become dominant as soon as the younger generation begins to form. Similarly, for any next aligned generation, its age is considered to be the age of the previous generation subtracted from the currently-investigated generation's buoyancy timescale.

⁷<http://leda.univ-lyon1.fr/>

3.3.2 Uncertainties in cavity ages

For the sound-speed timescale, the temperature (kT) at cavity distance d was established by interpolating between the values of the temperature radial profile. The resulting uncertainty was established as the root of the sum of the squares of the interpolation uncertainty and the radial kT profile's closest point to the interpolated value.

Regarding the buoyancy timescale, we assumed that if the volume V changes by a factor of two, the cross-sectional area changes proportionally. In our work, we first established that $V/S \sim R_1$ and then considered, that if the upper limit of a volume estimate is $2V$ with each direction changing equally with a factor of η , then one direction, e.g., R_1 , changes with a factor of $\eta = 2^{1/3}$. Similarly, it can be easily shown that for negative uncertainty $V/2$, R_1 scales with $\eta = 0.5^{1/3}$. Therefore, we considered the buoyancy uncertainties to be

$$v_{\text{buo}+} = 2^{1/6} v_{\text{buo},0}, \text{ and } v_{\text{buo}-} = 0.5^{1/6} v_{\text{buo},0}. \quad (3.6)$$

Buoyancy timescale relative uncertainty was then considered to be the same as for the buoyancy speed, therefore deducing the absolute uncertainties from basic knowledge of uncertainty relations.

3.4 Jet powers

Jet powers are commonly estimated from measured energy – i.e., the cavity's enthalpy H , and either its sound-speed timescale t_{ss} or buoyancy timescale t_{buo} . This approach, assuming the injected energy E_{inj} equals the measured energy E_{mea} , underestimates the jet powers due to the omission of the energy exchanged with the surrounding gas when the cavity rises through the atmosphere.

To take the exchange of energy into account, we considered the injected energy to be $E_{\text{inj}} = E_{\text{mea}} + \Delta E$, where we substituted for ΔE from Eq. 2.7. Injected energy was then considered to be

$$E_{\text{inj}} = E_{\text{mea}} \left[\frac{p_0}{p} \right]^{1-1/\gamma}, \quad (3.7)$$

where E_{mea} is the cavity's enthalpy H , p_0 is the central pressure⁸, and γ is 4/3. Cavity ages t_{age} were used as time t in Eq. 2.5.

To our current knowledge, there has not been a study proving or disproving any particular trends when it comes to the time evolution of jet powers in multi-cavity systems. Due to the self-regulatory nature of AGN feedback, we expect the jet powers per cavity generation to oscillate around a constant value. To probe the constancy of jet powers, we calculated the cycle-corrected time-averaged jet power as

$$\widetilde{P}_{\text{jet}} = \frac{\sum_{i=1}^N E_{\text{inj},i}}{t_{\text{age},o}}, \quad (3.8)$$

where $E_{\text{inj},i}$ is the energy injected into the i -th generation and $t_{\text{age},o}$ is the cavity age of the oldest generation.

⁸Throughout this work, we used the pressure measured in the innermost spectral annulus.

3.5 Inclination

3.5.1 Toy bubbles

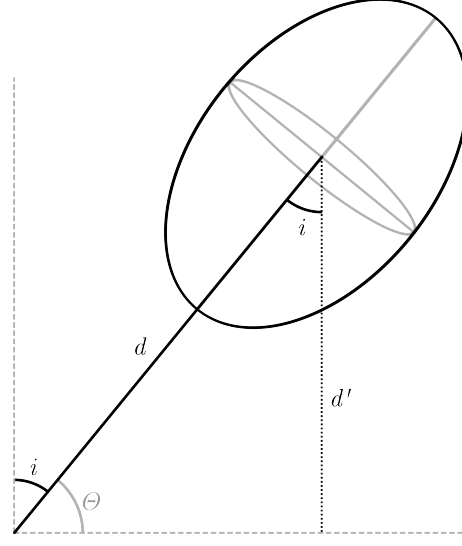


Figure 3.2: Inclination's effect on cavity's distance.

Firstly, inclination directly affects the projected distance of the cavity from the galactic centre. As can be seen in the Fig. 3.2, projected distance d' can be determined as

$$d' = d \cos i, \quad (3.9)$$

where d is the intrinsic cavity distance.

As for the cavity's shape, Guo (2020) found that inclination does not change the oblate cavity into prolate and vice versa. The study also derived relation between projected radial elongation τ' and intrinsic radial elongation τ as

$$\begin{aligned} \tau' &= \sqrt{\cos^2 \theta + \tau^2 \sin^2 \theta} \\ &= \sqrt{\sin^2 i + \tau^2 \cos^2 i}. \end{aligned} \quad (3.10)$$

For projected semi-axis R'_1 we get

$$R'_1 = R_w \sqrt{\sin^2 i + \tau^2 \cos^2 i}. \quad (3.11)$$

To probe how cavity characteristics would change if we inclined the system, we created a toy model of an oblate and a prolate cavity placed into atmosphere, whose temperature T was constant, electron density profile $n_e(r)$ was described by a deprojected β -model and so was the pressure profile $p(r)$. The intrinsic values were taken to be the ones at $i = 0^\circ$, and the end-point for inclination change was considered to be 60° . At the inclination of 60° , the cavity was considered to be nearly undetectable due to low contrast compared to the surrounding gas. Moreover, Plšek et al. (2023) investigated the cavity volume errors in relation to launching angle and found that at inclination angle $\sim 60^\circ$, the volumes are underestimated by at least 20% (Fig. 10, therein) and for even bigger angles, the error rapidly increases.

3.5.2 Studied cavities

Inclination affecting our measurements was then used to explain why the jet power is not constant across generations in some systems. We considered the cavity generation to be already inclined by some angle i , therefore, we knew its projected distance d' and its projected semi-axis R'_1 . Then, we figured out the intrinsic distance d and semi-axis R_1 and used them to establish the intrinsic jet power P_{jet} needed to inflate the cavity.

3.6 Misalignments

As was mentioned in Sect. 2.3, a strong misalignment between generations can be explained by the precession of the jet excavating the bubble. To probe if either of the scenarios could be plausible, we modelled various precession set-ups described in a study by Britzen et al. (2018).

Firstly, due to the misalignment between the angular momentum of the rotating black hole and of the accretion disc, the Lense-Thirring precession of the black hole may arise with the precession period

$$P_{\text{LT,BH}} = 10^{9.25} a_{\bullet}^{5/7} \alpha_{\text{vis}}^{48/35} \left(\frac{M_{\bullet}}{10^8 M_{\odot}} \right)^{1/7} \left(\frac{\dot{M}_{\bullet}}{10^{-2} M_{\odot} / \text{yr}} \right)^{-6/5} \text{ yr}, \quad (3.12)$$

where a_{\bullet} is the Kerr angular momentum parameter, α_{vis} is the viscosity parameter, M_{\bullet} is the mass of the SMBH and \dot{M}_{\bullet} its accretion rate (Lu Ju-fu, 1992).

In the case of Lense-Thirring precession of the accretion disc, the precession period depends on the BH's angular momentum, the size of the accretion disc's precessing part, and the accretion disc's surface density⁹. The precession period of the accretion disc was modelled according to (Caproni et al., 2004) as

$$P_{\text{LT,AD}} = \frac{2\pi G M_{\bullet}}{c^3} \frac{\int_{\xi_{\text{in}}}^{\xi_{\text{out}}} \frac{d\xi}{\xi^{3/2+a_0}}}{\int_{\xi_{\text{in}}}^{\xi_{\text{out}}} \xi \frac{1 - (1 - 4a_{\bullet} \xi^{-3/2} + 3a_{\bullet}^2 \xi^{-2})^{1/2}}{[\xi^{3/2} + a_{\bullet}]^{-2}} d\xi}, \quad (3.13)$$

where

$$\begin{aligned} \xi_{\text{in}} &= \xi_{\text{ms}} = 3 + A_2 \mp [(3 - A_1)(3 + A_1 + 2A_2)]^{1/2}, \\ A_1 &= 1 + (1 - a_{\bullet}^2)^{1/3} [(1 + a_{\bullet})^{1/3} + (1 - a_{\bullet})^{1/3}], \quad A_2 = (3a_{\bullet}^2 + A_1^2)^{1/2} \quad \text{and} \\ \xi_{\text{out}} &= \chi \xi_{\text{ms}}. \end{aligned}$$

The extent of the precessing part of the disc is given by dimensionless parameters ξ_{in} and ξ_{out} . The parameters are physical radii scaled with respect to gravitational radius as $\xi_{\text{in}} = R_{\text{in}}/R_g$ and $\xi_{\text{out}} = R_{\text{out}}/R_g$. The outer disc radius was considered to be $100R_{\text{in}}$, with R_{in} corresponding to the marginally stable orbit of a Kerr black hole.

In the case of a binary BH, a possible misalignment between the orbital plane and the accretion disc can also lead to the jet precession. The outer disc radius $r_{\text{d}}^{\text{out}}$ needs to

⁹For the sake of simplicity, constant surface density was considered.

be smaller than the distance between the BBH components. The resulting parameters can then decide the plausibility of the model. The outer disc radius was calculated as

$$r_d^{\text{out}} = \left[\frac{8\pi}{3} \left(\frac{5-n}{7-2n} \right) \frac{(1+z)}{P_{\text{prec}} \cos \Omega} \frac{r_{\text{ps}}^3}{\sqrt{GM_{\text{tot}}}} \right]^{2/3} \frac{x_p^{1/3}}{(1-x_p)^{2/3}}, \quad (3.14)$$

where n is the polytropic index of the gas, z the system's redshift, P_{jet} the desired precession period, Ω the inclination angle of the orbital plane to the accretion disc and x_p the ratio of the primary BH's mass M_1 to the total mass of the system $M_{\text{tot}} = M_1 + M_2$ (Britzen et al., 2018; Papaloizou and Terquem, 1995; Larwood, 1997).

Chapter 4

Results

We have analysed archival *Chandra X-ray Observatory* data for four nearby giant elliptical galaxies that are known to have multiple generations of X-ray cavities: NGC 5813, NGC 5044, NGC 4649 and NGC 4472.

To infer the temperature and electron density profiles, spectra from annular regions were extracted and fitted by a model combining the emission of collisional ionised plasma and bremsstrahlung emission. Concentric annular regions were centred at the X-ray emission peak set by a centroid in *DS9*. For each annulus, we combined all spectral files together, and the combined spectra were binned via the *ftgrouppha* command. Setting the type of grouping as *optmin*, the spectra were either binned by an optimal number of counts or by 25 counts. If not stated otherwise, the spectra were subsequently deprojected and fitted in the energy range of 0.7 – 7 keV and bremsstrahlung emission was fitted throughout every annulus, although its contribution was significant only in the central regions. Abundances of neighbouring annuli were tied, thus creating only about three or four sectors for abundance fitting.

Image analysis was performed to identify cavities in each system. Initially, a single β -model was fitted and subtracted from the image. In cases where a single β -model inadequately described the surface brightness radial profile of the source, a double β -model was applied. Cavities were then identified and estimated as ellipsoidal regions in the resulting residual image. Alternatively, cavities were identified by the machine-learning pipeline CADET. In CADET, various scales were employed to detect the cavities while maintaining the best possible pixel resolution, thus getting more precise estimates for cavity semi-axis and volume. The threshold for cavity decomposition was set to be 0.6 or 0.5.

Tab. 4.1 and Tab. 4.2 summarise the cavities and their properties identified by subtracting a β -model or applying CADET, respectively. For identified cavities, we used a notation system that begins with the letter *G*, followed by the generation's order from the centre out and the indicator of its direction in the plane of the sky.

4.1 NGC 5813

Spectra were extracted from concentric annular regions extending to $120''$ from the centre of the galaxy. Bremsstrahlung emission was fitted only for the inner four regions. Deprojected radial profiles of temperature and electron density are shown in Fig. 4.1.

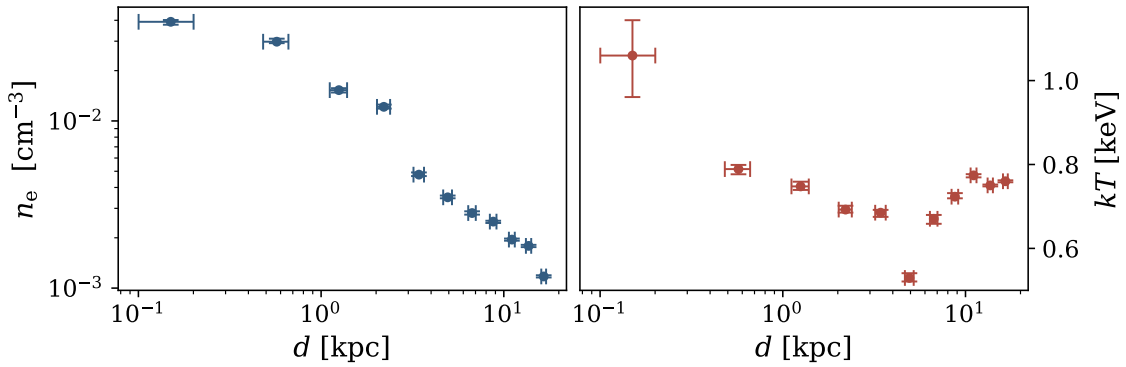


Figure 4.1: Deprojected electron density and temperature radial profiles for NGC 5813.

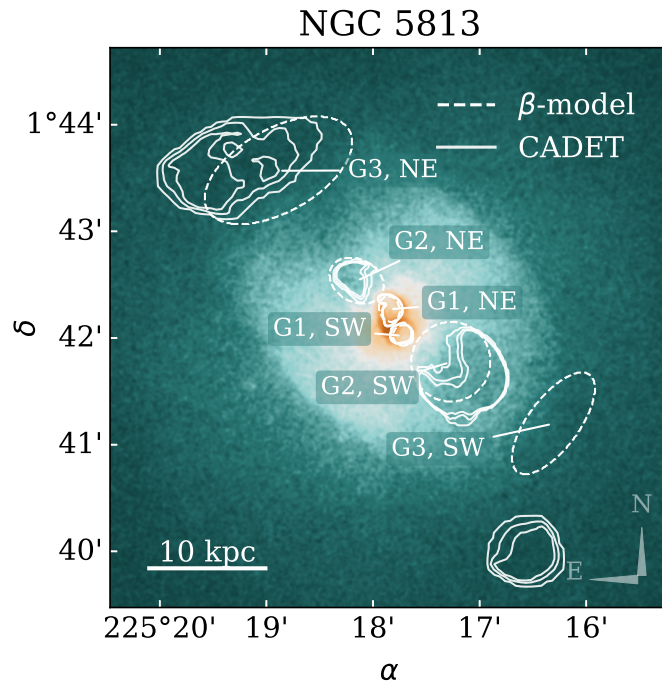


Figure 4.2: Broad band exposure-corrected image of NGC 5813 overlaid with cavity contours identified by β -modelling and CADET. The image was convolved with a Gaussian kernel with $\sigma = 1.5$.

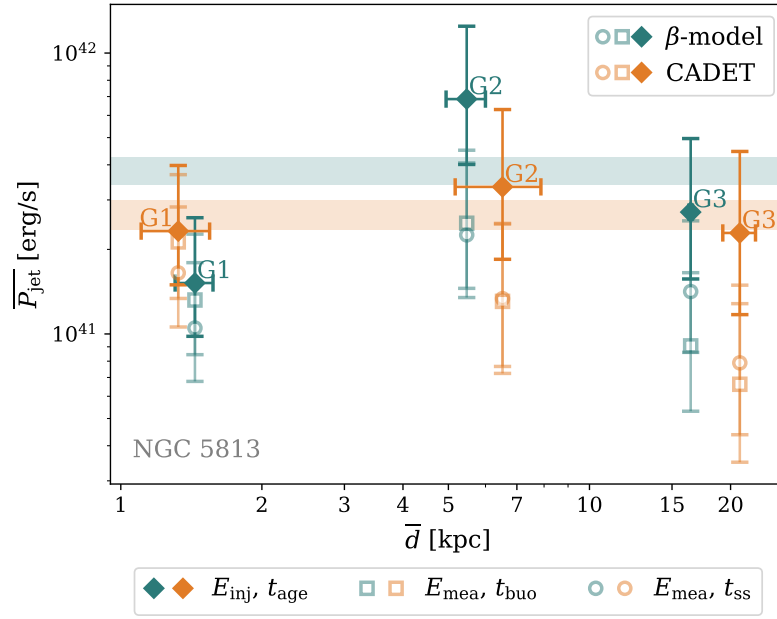


Figure 4.3: Cumulative jet power per cavity generation $\overline{P}_{\text{jet}}$ as a function of average distance of cavities \overline{d} . Shaded blue and orange areas note the upper and lower limit of time-averaged cycle-corrected jet power (Eq. 3.8) for β -model and CADET cavities, respectively.

β -modelling and CADET revealed three generations of cavities in the atmosphere of NGC 5813. Their positions and shapes are depicted in Fig. 4.2. Elliptical regions identified as cavities after β -modelling and CADET contours coincide well for the inner two generations. For the outermost cavity in the SW direction, CADET contours deviate significantly compared to the ellipse regions resulting from β -modelling. The difference from CADET contours is most likely caused by CADET's inability to deal with chip edges and the fact that the training dataset focused on the inner generations.

We applied timescales and energy corrections and compared them with the usual approach, as can be seen in Fig. B.1 and Fig. B.2. Plotting the cumulative $\overline{P}_{\text{jet}}$, i.e., the sum of energy injected into both cavities divided by the average cavity age in the generation t_{age} , we can see that $\overline{P}_{\text{jet}}$ roughly follows a constant value.

4.2 NGC 5044

Spectra were extracted from 11 concentric annuli. The two innermost annuli were tied for the temperature fitting. Bremsstrahlung emission was fitted throughout every annulus. Radial profiles are shown in Fig. 4.4.

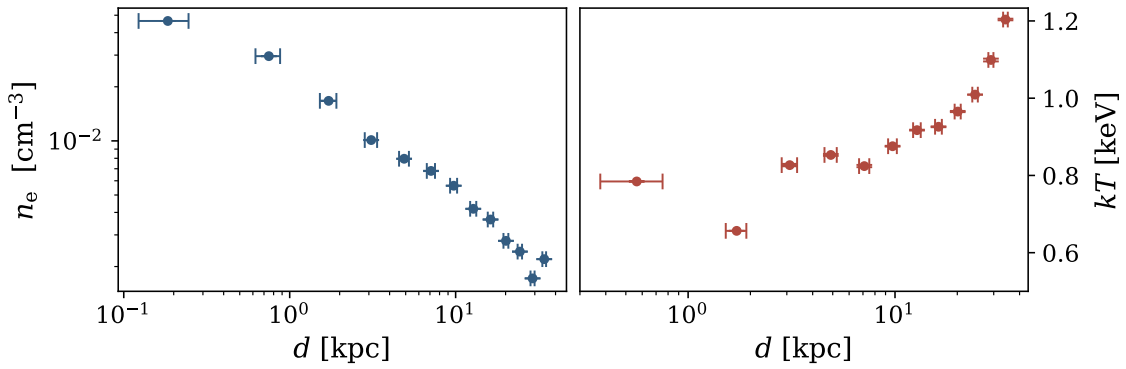


Figure 4.4: Electron density and temperature radial profiles for NGC 5044.

Three generations were identified in the NGC 5044 both by β -modelling and CADET, Fig. 4.5 presents their position and extent. Two of them (G1, G2) are nicely aligned in the N-S direction. A misaligned generation (M) is found in the NE-SW direction. Interestingly, the cavity in the SW direction of the misaligned generation is closer than its counterpart. The misaligned generation (M) and outermost aligned generation (G2) seem to be of similar age, yet the jet power that was needed to excavate the G2 cavities was by an order of magnitude larger.

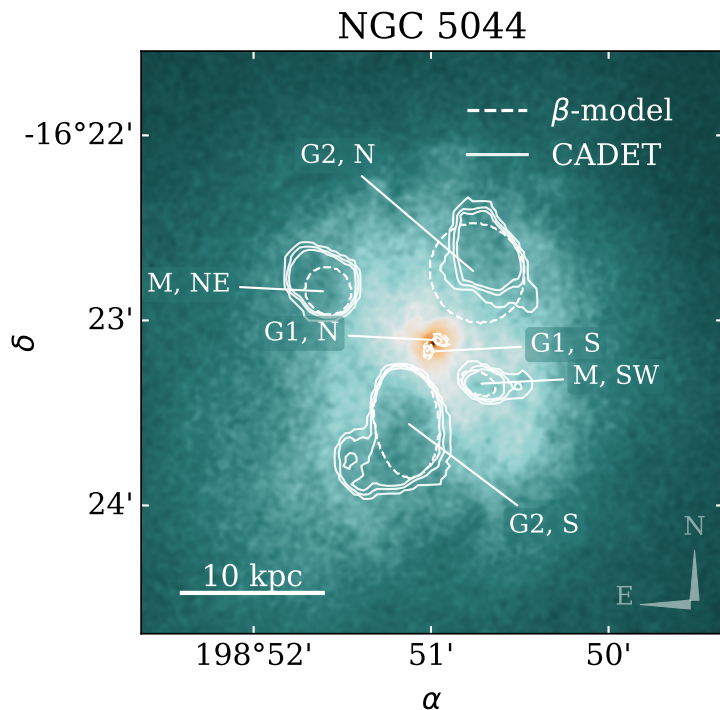


Figure 4.5: Broad band exposure-corrected image of NGC 5044 overlaid with cavity shapes identified by β -modelling and CADET. The image was convolved with a Gaussian kernel with $\sigma = 1.5$.

Concerning cycle-corrected time-averaged jet power $\widetilde{P}_{\text{jet}}$, Fig. 4.6 demonstrates that G2 distorts $\widetilde{P}_{\text{jet}}$ towards the higher values and thus $\overline{P}_{\text{jet}}$ does not appear to be constant throughout multiple cycles.

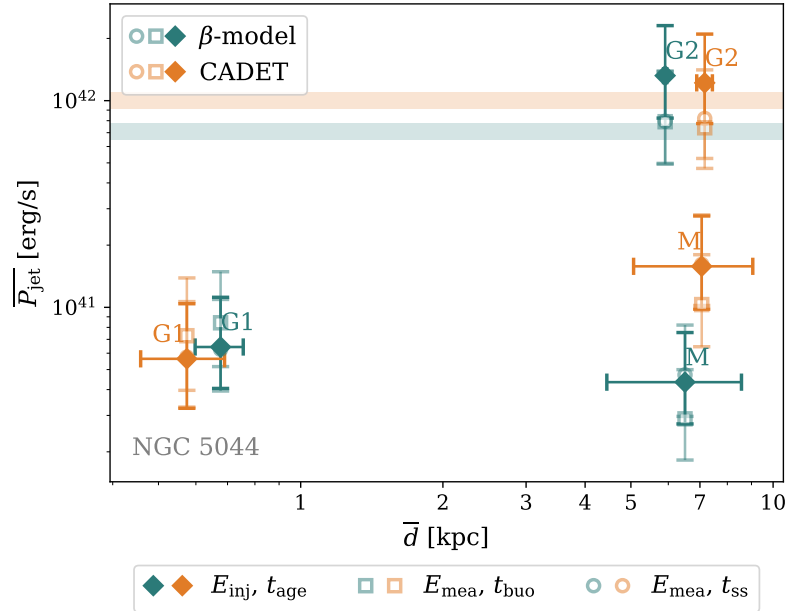


Figure 4.6: Cumulative jet power per generation $\overline{P}_{\text{jet}}$ in NGC 5044 as a function of average distance of cavities \bar{d} . Shaded areas note the upper and lower limit for time-averaged cycle-corrected $\widetilde{P}_{\text{jet}}$ calculated according to Eq. 3.8. Orange colour denotes the CADET identification, blue the β -model identification.

4.3 NGC 4649

Spectral analysis was performed for spectra from 11 concentric annular regions centred at the X-ray emission peak and extending to about 200'' from the centre. Besides abundance, no parameters were tied together for the neighbouring annuli. Fig. 4.10 depicts the resulting deprojected radial profiles for electron density and temperature.

Although CADET identified only the inner cavity generation, visual inspection hinted at the second generation about 20 kiloparsecs from the centre, as is illustrated in Fig. B.5. The cavities are well aligned with the NE-SW direction, true to the galaxy being known as one of the most symmetric ones.

Figures B.5 and B.6 compare the classical approach to timescale and energy calculations, respectively, and the newly-introduced methods. Resulting cumulative jet powers $\overline{P}_{\text{jet}}$ are shown in Fig. 4.9. Time-averaged cycle-corrected jet power $\widetilde{P}_{\text{jet}}$ was calculated only for the β -model cavities.

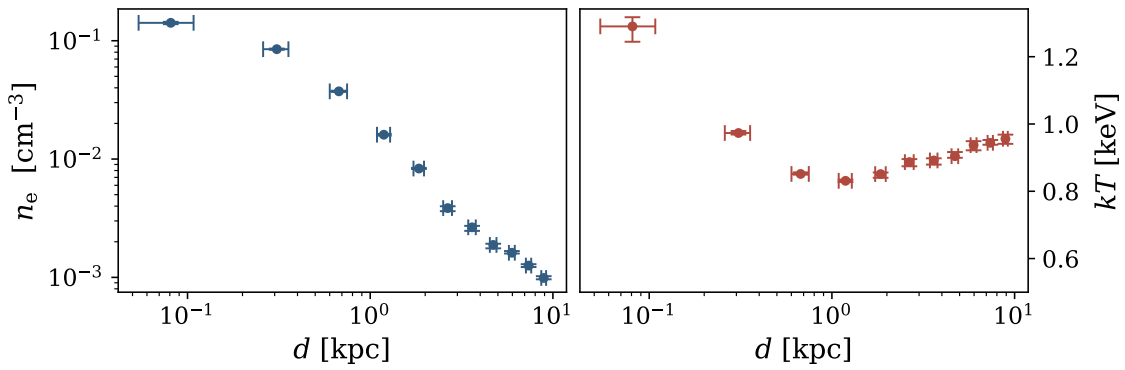


Figure 4.7: Electron density and temperature profiles for NGC 4649.

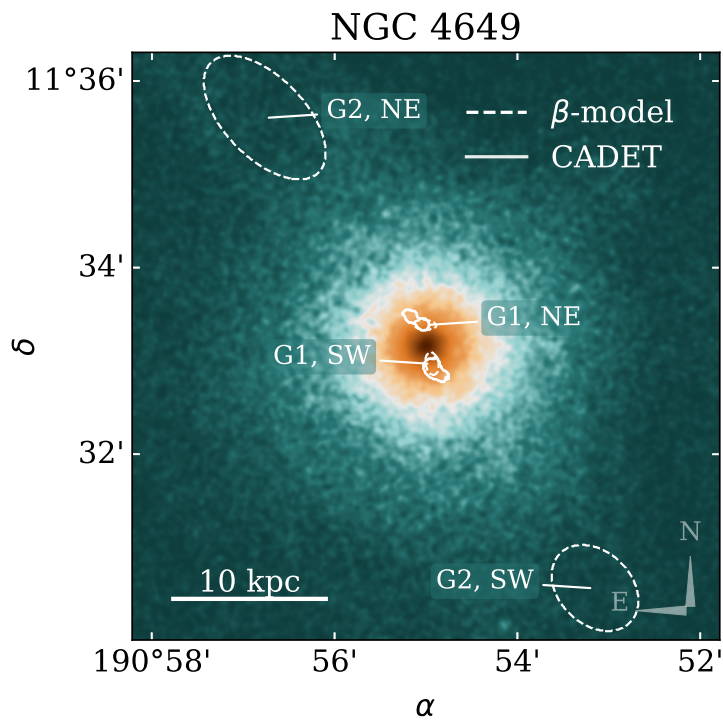


Figure 4.8: Broad band exposure-corrected image of NGC 4649 overlaid with cavity contours identified by β -modelling and CADET. The fits file was convolved with a Gaussian kernel with $\sigma = 3$.

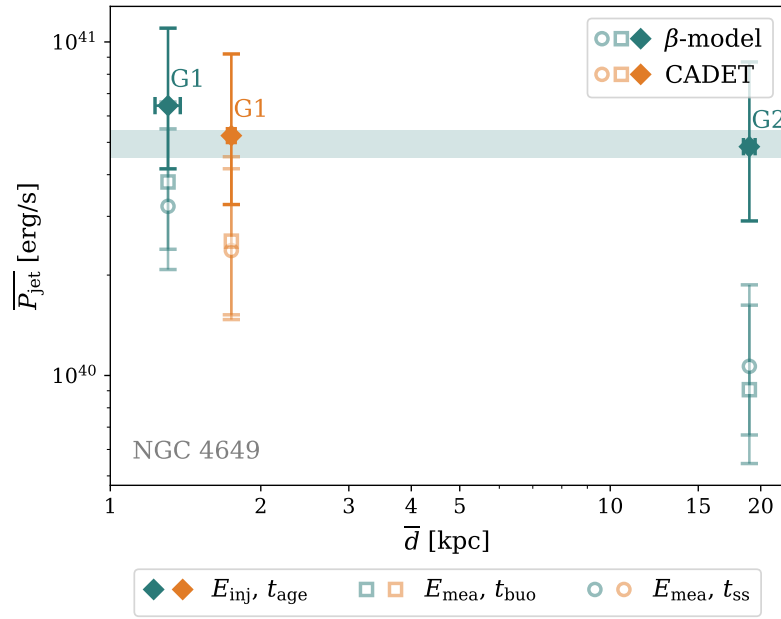


Figure 4.9: Cumulative jet power per generation P_{jet} in NGC 4649 as a function of average cavity distance \bar{d} with $\widetilde{P}_{\text{jet}}$ calculated from Eq.3.8 denoted by shaded areas (blue for β -model cavities, orange for CADET cavities).

4.4 NGC 4472

Spectra extracted from 11 annuli extending to about 200" from the centre were deprojected and fitted. The obtained electron density and temperature radial profiles are shown in Fig. 4.10.

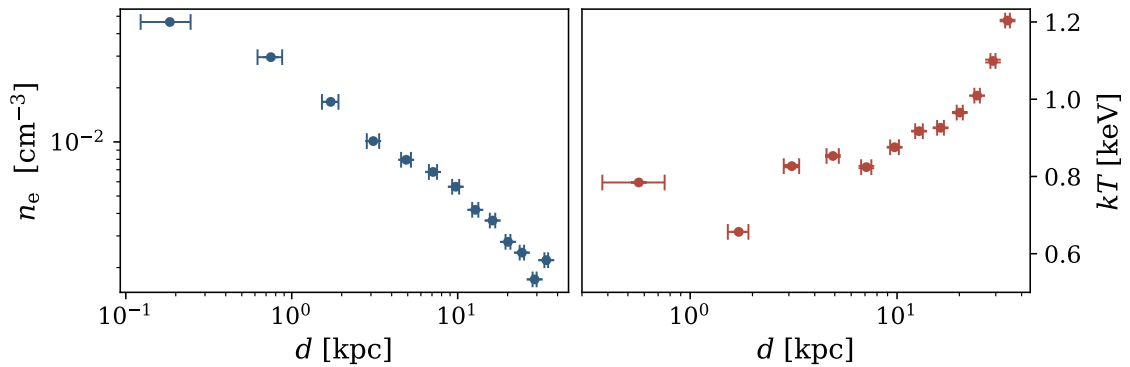
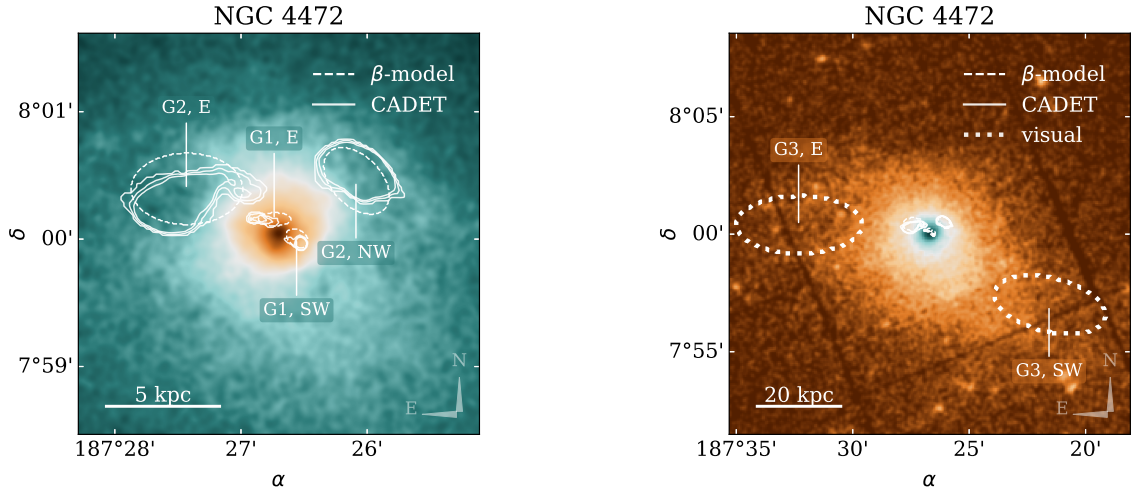


Figure 4.10: Electron density and temperature radial profiles for NGC4472.

Two generations were identified via image analysis performed on *Chandra* data by both β -modelling and CADET. Seeing a hint of a third generation in an *XMM-Newton* data about 30 kiloparsecs from the centre, we experimentally incorporated it into our calculations. The application of a new approach to calculating the cavity ages and en-

ergetics is illustrated in Fig. B.7 and Fig. B.8, respectively. Cumulative jet powers per cavity generation are shown in Fig. 4.12.



(a) *Chandra* soft band exposure-corrected image of NGC 4472 overlaid with cavity contours identified by β -modelling and CADET. The fits file was convolved with a Gaussian kernel with $\sigma = 3$.

(b) *XMM-Newton*'s EPIC MOS1 image accessed via *XMM-Newton* Science Archive. The fits file was convolved with a Gaussian kernel with $\sigma = 1$.

Figure 4.11: *Chandra* and *XMM-Newton* images of NGC4472.

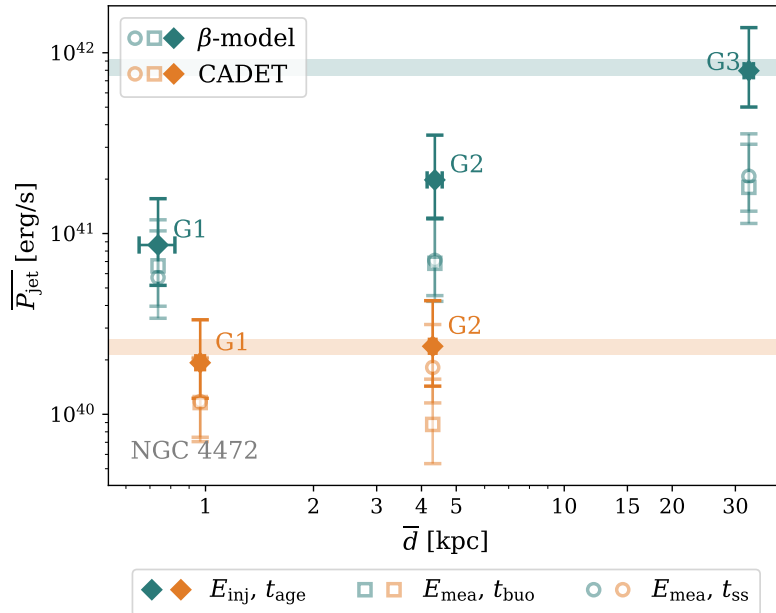


Figure 4.12: Cumulative jet power per generation $\overline{P}_{\text{jet}}$ in NGC 4472 as a function of average cavity distance \overline{d} with $\overline{P}_{\text{jet}}$ calculated from Eq. 3.8 denoted by blue and orange shaded areas, corresponding to β -model and CADET cavities, respectively.

Table 4.1: Cavity characteristics of cavities identified from β -modelling.

Galaxy	Cavity	d [kpc]	R_1 [kpc]	R_w [kpc]	τ	φ_{pos} [°]	φ_{rot} [°]	t_{age} [Myr]	E_{mea} [erg]	E_{inj} [erg]
NGC 5813	G1, NE	1.57	1.12	0.86	1.30	93.0	12.5	3.70 ^{+0.03} _{-0.03}	5.7 ^{+5.7} _{-2.9} · 10 ⁵⁴	8.4 ^{+8.4} _{-4.2} · 10 ⁵⁴
	G1, SW	1.31	0.88	0.88	1.00	327.3	32.7	3.08 ^{+0.02} _{-0.02}	5.5 ^{+0.5} _{-0.3} · 10 ⁵⁵	0.8 ^{+0.8} _{-0.4} · 10 ⁵⁵
	G2, NE	4.94	2.46	1.83	1.34	125.9	26.4	7.2 ^{+1.6} _{-1.1}	1.9 ^{+1.9} _{-0.9} · 10 ⁵⁵	3.6 ^{+3.6} _{-1.8} · 10 ⁵⁵
	G2, SW	6.00	3.40	3.43	0.99	330.3	86.4	9.3 ^{+1.9} _{-1.2}	7.6 ^{+7.6} _{-3.8} · 10 ⁵⁵	1.54 ^{+1.5} _{-0.8} · 10 ⁵⁶
	G3, NE	16.58	3.58	7.0	0.51	125.5	83.7	48.3 ^{+9.3} _{-6.8}	1.2 ^{+1.2} _{-0.6} · 10 ⁵⁶	3.2 ^{+3.2} _{-1.6} · 10 ⁵⁶
	G3, SW	16.3	2.19	5.2	0.42	329.5	96.1	59.8 ^{+11.0} _{-7.7}	4.3 ^{+4.3} _{-2.1} · 10 ⁵⁵	1.1 ^{+1.1} _{-0.6} · 10 ⁵⁶
NGC 5044	G1, N	0.60	0.66	0.34	1.92	14.0	41.8	1.307 ^{+0.001} _{-0.001}	1.71 ^{+1.7} _{-0.9} · 10 ⁵⁴	1.7 ^{+1.7} _{-0.9} · 10 ⁵⁴
	G1, S	0.76	0.61	0.31	1.93	240.4	29.6	1.683 ^{+0.001} _{-0.001}	1.13 ^{+1.1} _{-0.6} · 10 ⁵⁴	1.2 ^{+1.2} _{-0.6} · 10 ⁵⁴
	G2, N	5.86	3.30	3.58	0.92	56.1	60.3	11.4 ^{+1.9} _{-1.3}	2.1 ^{+2.1} _{-1.0} · 10 ⁵⁶	3.07 ^{+3.07} _{-1.5} · 10 ⁵⁶
	G2, S	5.95	4.06	2.27	1.79	250.7	25.4	10.1 ^{+1.8} _{-1.2}	1.02 ^{+1.02} _{-0.51} · 10 ⁵⁶	1.5 ^{+1.5} _{-0.8} · 10 ⁵⁶
	M, NE	8.57	1.73	1.6	1.08	155.1	32.2	31.1 ^{+4.7} _{-3.1}	1.7 ^{+1.7} _{-0.85} · 10 ⁵⁵	2.7 ^{+2.7} _{-1.3} · 10 ⁵⁵
	M, SW	4.45	1.30	0.79	1.64	318.6	16.9	13.4 ^{+2.0} _{-1.3}	4.9 ^{+4.9} _{-2.4} · 10 ⁵⁴	6.8 ^{+6.8} _{-3.4} · 10 ⁵⁴
NGC 4649	G1, NE	1.38	0.31	0.75	0.42	94.8	79.9	2.875 ^{+0.006} _{-0.006}	1.5 ^{+1.5} _{-0.7} · 10 ⁵⁴	3.0 ^{+3.0} _{-1.5} · 10 ⁵⁴
	G1, SW	1.23	0.75	0.43	1.76	288.1	8.2	2.567 ^{+0.005} _{-0.005}	1.3 ^{+1.3} _{-0.7} · 10 ⁵⁴	2.6 ^{+2.6} _{-1.3} · 10 ⁵⁴
	G2, NE	18.47	5.04	2.64	1.91	125.9	8.4	36.3 ^{+5.9} _{-3.9}	8.3 ^{+8.3} _{-4.1} · 10 ⁵⁴	4.1 ^{+4.1} _{-2.1} · 10 ⁵⁵
	G2, SW	19.49	3.22	2.37	1.36	305.4	10.3	50.6 ^{+8.0} _{-5.3}	4.0 ^{+4.0} _{-2.0} · 10 ⁵⁴	2.0 ^{+2.0} _{-1.0} · 10 ⁵⁵
NGC 4472	G1, E	0.65	0.29	0.72	0.40	108.6	71.6	1.419 ^{+0.002} _{-0.002}	2.0 ^{+2.0} _{-1.0} · 10 ⁵⁴	3.0 ^{+3.0} _{-1.5} · 10 ⁵⁴
	G1, SW	0.82	0.52	0.36	1.45	344.8	20.0	1.788 ^{+0.002} _{-0.002}	0.7 ^{+0.7} _{-0.4} · 10 ⁵⁴	1.1 ^{+1.1} _{-0.6} · 10 ⁵⁴
	G2, E	4.57	2.46	1.58	1.56	154.6	25.4	6.70 ^{+1.2} _{-0.8}	1.2 ^{+1.2} _{-0.6} · 10 ⁵⁵	2.9 ^{+2.9} _{-1.4} · 10 ⁵⁵
	G2, NW	4.15	1.09	1.75	0.62	33.9	79.9	8.7 ^{+1.6} _{-1.1}	7.2 ^{+7.2} _{-3.6} · 10 ⁵⁴	1.7 ^{+1.7} _{-0.8} · 10 ⁵⁵
	G3, E	31.73	15.08	6.86	2.20	176.7	3.3	53.2 ^{+9.2} _{-6.2}	2.1 ^{+2.1} _{-1.0} · 10 ⁵⁶	8.0 ^{+8.0} _{-4.0} · 10 ⁵⁶
	G3, SW	33.69	13.62	6.41	2.12	329.0	17.6	60.2 ^{+10.6} _{-7.2}	1.5 ^{+1.5} _{-0.8} · 10 ⁵⁶	6.1 ^{+6.1} _{-3.0} · 10 ⁵⁶

Table 4.2: Cavity characteristics of cavities identified by CADET.

Galaxy	Cavity	d [kpc]	R_l [kpc]	R_w [kpc]	τ	ϕ_{prot} [°]	t_{age} [Myr]	E_{mea} [erg]	E_{inj} [erg]
NGC 5813	G1, NE	1.11	0.98	0.89	1.10	-7.1	$2.58^{+0.02}_{-0.02}$	$7.8^{+7.8}_{-3.9} \cdot 10^{54}$	$1.1^{1.1}_{-0.5} \cdot 10^{55}$
	G1, SW	1.55	0.91	1.36	0.67	102.1	$3.64^{+0.03}_{-0.03}$	$7.9^{+7.9}_{-4.0} \cdot 10^{54}$	$1.2^{1.2}_{-0.6} \cdot 10^{55}$
	G2, NE	7.88	3.11	3.83	0.81	54.5	$15.3^{+2.7}_{-1.8}$	$6.4^{+6.4}_{-3.2} \cdot 10^{55}$	$1.4^{1.4}_{-0.7} \cdot 10^{56}$
	G2, SW	5.17	1.46	1.65	0.88	126.5	$11.0^{+2.2}_{-1.5}$	$8.2^{+8.2}_{-4.1} \cdot 10^{54}$	$1.6^{1.6}_{-0.8} \cdot 10^{55}$
	G3, NE	22.61	3.0	2.88	1.04	15.2	$77.0^{+14.3}_{-9.8}$	$1.49^{+1.5}_{-0.7} \cdot 10^{55}$	$4.2^{4.2}_{-2.1} \cdot 10^{55}$
	G3, SW	19.25	6.46	3.44	1.88	19.4	$38.7^{+8.6}_{-6.3}$	$9.6^{+9.6}_{-4.8} \cdot 10^{55}$	$2.6^{2.6}_{-1.3} \cdot 10^{56}$
NGC 5044	G1, N	0.46	0.27	0.43	0.63	130.2	$0.981^{+0.001}_{-0.001}$	$1.5^{+1.5}_{-0.7} \cdot 10^{54}$	$1.5^{1.5}_{-0.7} \cdot 10^{54}$
	G1, S	0.69	0.26	0.28	0.93	99.8	$1.525^{+0.001}_{-0.001}$	$4.5^{+4.5}_{-2.2} \cdot 10^{53}$	$4.6^{4.6}_{-2.3} \cdot 10^{53}$
	G2, N	7.44	3.36	4.68	0.72	61.1	$16.6^{+2.6}_{-1.8}$	$2.3^{+2.2}_{-1.2} \cdot 10^{56}$	$3.6^{3.6}_{-1.8} \cdot 10^{56}$
	G2, S	6.89	2.38	3.75	0.63	121.2	$13.6^{+2.3}_{-1.5}$	$15.11^{+15.1}_{-7.6} \cdot 10^{55}$	$22.9^{22.9}_{-11.4} \cdot 10^{55}$
	M, NE	5.07	2.41	1.21	1.99	-6.2	$16.7^{+2.5}_{-1.7}$	$2.0^{+2.0}_{-1.0} \cdot 10^{55}$	$2.8^{+2.8}_{-1.4} \cdot 10^{55}$
	M, SW	9.06	2.91	2.36	1.23	-40.5	$28.9^{+4.3}_{-2.9}$	$6.0^{+6.0}_{-3.0} \cdot 10^{55}$	$9.5^{+9.5}_{-4.8} \cdot 10^{55}$
NGC 4649	G1, NE	1.8	0.94	0.35	2.65	-34.2	$3.68^{+0.02}_{-0.02}$	$8.4^{+8.4}_{-4.2} \cdot 10^{53}$	$1.9^{+1.9}_{-0.9} \cdot 10^{54}$
	G2, SW	1.7	0.89	0.54	1.67	-44.7	$3.55^{+0.02}_{-0.02}$	$1.8^{+1.8}_{-0.9} \cdot 10^{54}$	$4.1^{+4.1}_{-2.0} \cdot 10^{54}$
NGC 4472	G1, E	0.99	6.72	2.39	2.81	-13.0	$2.133^{+0.003}_{-0.003}$	$3.0^{+3.0}_{-1.5} \cdot 10^{53}$	$4.9^{+4.9}_{-2.4} \cdot 10^{53}$
	G1, SW	0.94	4.44	2.65	1.68	-15.5	$2.025^{+0.003}_{-0.003}$	$4.7^{+4.7}_{-2.4} \cdot 10^{53}$	$7.7^{+7.7}_{-3.8} \cdot 10^{54}$
	G2, E	4.39	28.56	12.44	2.30	12.9	$21.5^{+3.5}_{-2.4}$	$1.9^{+1.9}_{-0.9} \cdot 10^{54}$	$4.4^{+4.4}_{-2.2} \cdot 10^{54}$
	G2, NW	4.21	19.72	11.88	1.66	-23.7	$12.6^{+2.2}_{-1.5}$	$2.9^{+2.9}_{-1.5} \cdot 10^{54}$	$6.9^{+6.9}_{-3.4} \cdot 10^{55}$

Table 4.3: Cavity jet powers.

Galaxy	Cavity	$P_{\text{jet}, \beta}$ [erg/s]	$P_{\text{jet}, c}$ [erg/s]
NGC 5813	G1, NE	$7.2^{+7.2}_{-3.6} \cdot 10^{40}$	$1.3^{+1.3}_{-0.7} \cdot 10^{41}$
	G1, SW	$8.0^{+8.0}_{-4.0} \cdot 10^{40}$	$1.0^{+1.0}_{-0.5} \cdot 10^{41}$
	G2, NE	$1.6^{+1.6}_{-0.8} \cdot 10^{41}$	$2.9^{+2.9}_{-1.5} \cdot 10^{41}$
	G2, SW	$5.3^{+5.4}_{-2.7} \cdot 10^{41}$	$4.7^{+4.8}_{-2.4} \cdot 10^{40}$
	G3, NE	$2.1^{+2.2}_{-1.1} \cdot 10^{41}$	$1.7^{+1.8}_{-0.9} \cdot 10^{40}$
	G3, SW	$5.9^{+6.0}_{-3.0} \cdot 10^{40}$	$2.1^{+2.2}_{-1.1} \cdot 10^{41}$
NGC 5044	G1, N	$4.2^{+4.2}_{-2.1} \cdot 10^{40}$	$4.7^{+4.7}_{-2.3} \cdot 10^{40}$
	G1, S	$2.2^{+2.2}_{-1.1} \cdot 10^{40}$	$9.6^{+9.6}_{-4.8} \cdot 10^{39}$
	G2, N	$8.5^{+8.6}_{-4.4} \cdot 10^{41}$	$6.9^{+6.9}_{-3.5} \cdot 10^{41}$
	G2, S	$4.7^{+4.8}_{-2.4} \cdot 10^{41}$	$5.4^{+5.4}_{-2.7} \cdot 10^{41}$
	M, NE	$2.7^{+2.8}_{-1.4} \cdot 10^{40}$	$5.3^{+5.4}_{-2.7} \cdot 10^{40}$
	M, SW	$1.6^{+1.6}_{-0.8} \cdot 10^{40}$	$1.1^{+1.1}_{-0.5} \cdot 10^{41}$
NGC 4649	G1, NE	$3.3^{+3.3}_{-1.6} \cdot 10^{40}$	$1.6^{+1.6}_{-0.8} \cdot 10^{40}$
	G1, SW	$3.2^{+3.2}_{-1.6} \cdot 10^{40}$	$3.6^{+3.6}_{-1.8} \cdot 10^{40}$
	G2, NE	$3.6^{+3.6}_{-1.8} \cdot 10^{40}$	
	G2, SW	$1.3^{+1.3}_{-0.6} \cdot 10^{40}$	
NGC 4472	G1, E	$6.7^{+6.7}_{-3.3} \cdot 10^{40}$	$7.3^{+7.3}_{-3.6} \cdot 10^{39}$
	G1, SW	$2.0^{+2.0}_{-1.0} \cdot 10^{40}$	$1.2^{+1.2}_{-0.6} \cdot 10^{40}$
	G2, E	$1.4^{+1.4}_{-0.7} \cdot 10^{41}$	$6.5^{+6.6}_{-3.3} \cdot 10^{39}$
	G2, NW	$6.1^{+6.2}_{-3.2} \cdot 10^{40}$	$1.7^{+1.8}_{-0.9} \cdot 10^{40}$
	G3, E	$4.8^{+4.8}_{-2.5} \cdot 10^{41}$	
	G3, SW	$3.2^{+3.2}_{-1.6} \cdot 10^{41}$	

Chapter 5

Discussion

In this final chapter, we evaluate our approach to data analysis and calculations based on the obtained results both globally across our sample and then individually for each galaxy. In the second part, we present a toy model which was utilised to probe how inclination affects our measurements.

As it will be shown below, probing projection effects in the observed systems requires energy measurement as precise as possible, especially for the cavities that are further from the centre. The magnitude of the correction to the energy calculations as described by Eq. 2.7 is illustrated in Fig. 5.1. A *fractional energy change*, which we defined as $(E_{\text{inj}} - E_{\text{mea}})/E_{\text{mea}}$, was calculated for every cavity in our sample. Larger deviations from the usual method, where the injected energy is simply taken to be the cavity enthalpy, are observed for the more distant cavities, i.e., for those that detached sooner and therefore deposited more energy into the ambient medium.

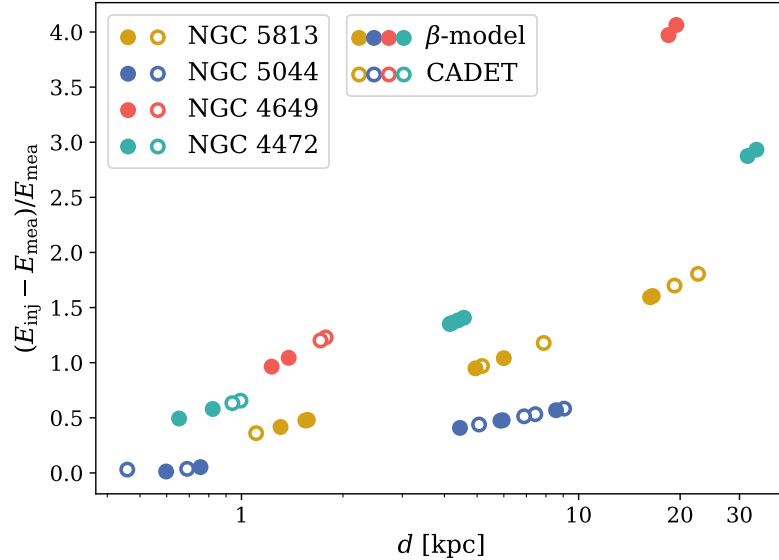


Figure 5.1: Fractional energy change $(E_{\text{inj}} - E_{\text{mea}})/E_{\text{mea}}$ for our sample of galaxies showcasing the influence of applied corrections to cavity energetics calculations described in Sect. 3.4.

5.1 Individual galaxies

5.1.1 NGC 5813

Our identification of three cavity generations agrees with the in-depth study done by [Randall et al. \(2015\)](#), although the position of the SW cavity in the second generation slightly disagrees with our work.

The system is strongly aligned, with positional angles differing only marginally in each direction. For the innermost generation, the cavities seem to be still attached and being inflated. The presence of bright shock rims enclosing the cavities also suggests ongoing cavity inflation. With increasing distance, the cavities are more azimuthally elongated. In [Fig. 4.3](#), we can see that having applied the timescale and energetics corrections mentioned in [Sect. 3.3.1](#) and [Sect. 3.4](#), respectively, the cumulative resulting jet powers per generation seem to be roughly equal to time-averaged cycle-corrected jet power (see [Eq. 3.8](#)). Thus, we can conclude that in this system, assuming that all cavities lie very nearly in the plane of the sky, the AGN outburst strength throughout the cycle seems to be constant.

5.1.2 NGC 5044

In [Fig. 4.6](#) we see that jet powers are not constant across the generations. The G2 cavities were seemingly inflated by a stronger jet whose jet power is by an order of magnitude larger compared to the other generations. However, our measurements can be skewed by the assumption that the cavity generation lies in the plane of the sky. To account for a possible inclination in calculating the intrinsic jet power, we assumed the generation to have some inclination and then recalculated what intrinsic value it corresponds to.

[Fig. 5.2](#) shows that the constant jet power can be reached if the system is projected from an inclination of at least 50° . However, if the cavity's inclination is close to or larger than 60° , the cavity will not be as prominent due to the low contrast. On the other hand, [Fig. 13](#) in [Giacintucci et al. \(2011\)](#) shows old radio emission in the galaxy NGC 5044, which extends toward the south and is absent in the north. This could potentially occur if the bipolar jets are inclined and, due to Doppler boosting, only one jet is visible.

[Schellenberger et al. \(2021\)](#) discovered a very young jet in NGC 5044, whose age was calculated to be ~ 1.7 kyr. It is strong evidence of an ongoing AGN activity, and we refer to the jet as the 0th generation.

To investigate whether the jet precession is the source of misalignment in NGC 5044, we probed different setups mentioned in [Sect. 3.6](#). For precession periods, we investigated 2 possibilities: between the 0th generation and the average age of the first generation ($P_{\text{prec},1} \sim 2.5$ Myr), and between the average ages of the second generation and the misaligned generation ($P_{\text{prec},2} \sim 23$ Myr). Precession periods were taken to be twice the difference between cavity ages, which were identified by β -modelling.

First, we modelled Lense-Thirring precession of the central BH for three different rotation parameters a_* ([Fig. 5.3](#)). Then we modelled Lense-Thirring precession of the

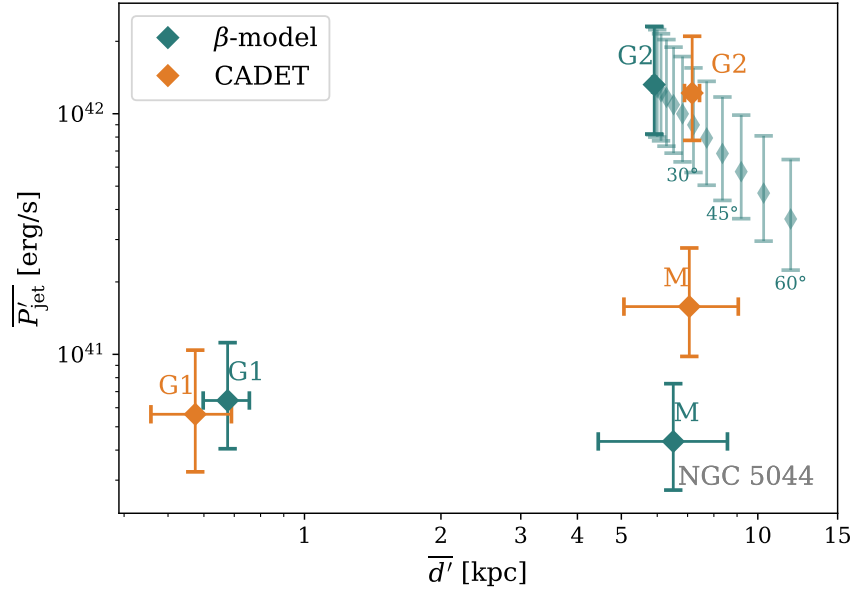


Figure 5.2: Projected cumulative jet powers $\overline{P}'_{\text{jet}}$ versus the average projected cavity generation distance \overline{d}' for NGC 5044. For the G1 and M generations, inclination was not accounted for, it was rather assumed that $\overline{P}'_{\text{jet}} = \overline{P}_{\text{jet}}$. Recalculated intrinsic cumulative $\overline{P}_{\text{jet}}$ for the second aligned generation (G2) from a presumed inclination are depicted by fainter data points.

accretion disc (Fig. 5.4) as a function of Eddington efficiency ϵ^1 . Lastly, we modelled the extent of the processing disc in the case of BBH (Fig. 5.5).

We can see that Lense-Thirring precession of a BH could be plausible if the BH rotated with a spin $a_\bullet \sim 0.01$ for $P_{\text{prec},1}$. A precession period of 23 Myr can be achieved if the BH's spin is described by $a_\bullet \sim 0.1$. For both precession periods, the Lense-Thirring precession of the accretion disc can be a viable precession mechanism under the assumption of a slowly spinning black hole.

Fig. 5.5 shows the outer disc radius of a precessing accretion disc due to the torques exerted by a companion BH as a function of the primary BH's mass fraction for a precession period of 2.5 million years. For this period, the separation of the primary and secondary constituents of a BBH r_{ps} is nearly 54 parsecs². On the other hand, if we calculate the radius of the sphere of influence r_{inf}^3 for a constituent BH, assuming the same mass of both BHs, r_{inf} is only 9 parsecs. Allowing for one constituent to be much heavier, the upper limit for r_{inf} is only about 18 parsecs. Thus, we can rule out the precession caused by torques from the secondary BH with a precession period of 2.5 million years. For a higher precession period, the observed trends in Fig. 5.5 shift towards higher $r_{\text{out}}^{\text{d}}$ and the corresponding r_{ps} reaches approximately 235 kpc, which is also implausible with the derived value of r_{inf} . On the other hand, if the constituents of BBH

¹For detailed explanation of calculations including the Eddington efficiency see Appendix C.

²Calculated from the Kepler law.

³ $r_{\text{inf}} = G M_\bullet / \sigma_v^2$ (Schneider, 2006). For the black hole mass M_\bullet calculation, see Appendix. C.

are closer, the precession period decreases, and the observed misalignments could develop after multiple precession cycles, rather than after a single cycle as assumed in the initial calculations.

A few words of caution should be added. Firstly, we only assumed one particular generation to be inclined. However, there is a chance that other generations are also inclined. For the precession periods, we took an average age of the cavity generations. Looking closely at the M generation, we see that there is a huge age difference between the individual cavities and the averaged value can skew the precession period estimate. We also assumed that the precession cone's axis lies in the plane of the sky and the opening angle of the cone corresponds to the angle between the galactocentric directions of the two generations, and thus, presuming the precession period to be twice the generations' age difference.

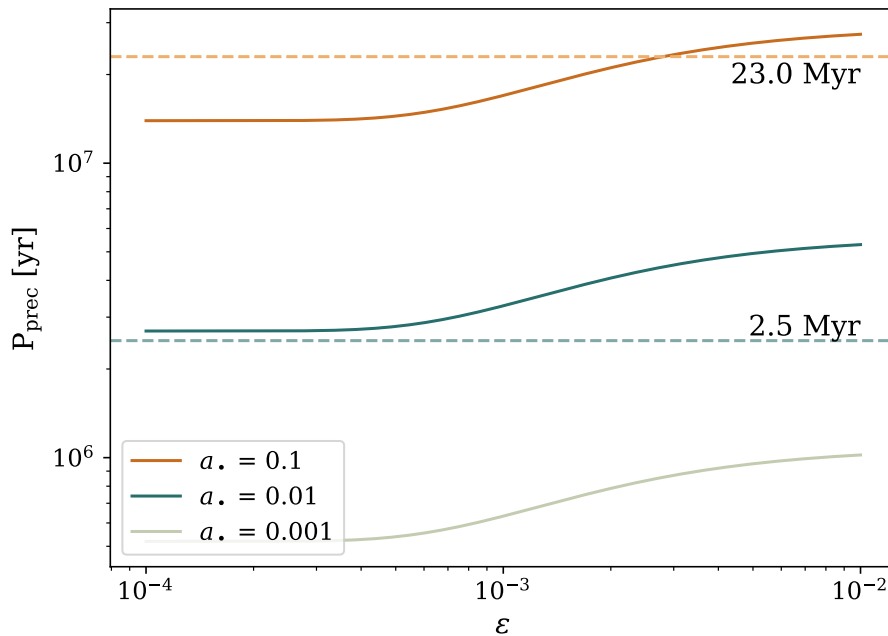


Figure 5.3: Lense-Thirring precession of a BH modelled for various rotation parameter a_* shown as a function of a fraction of the Eddington limit. Dashed lines represent the precession periods derived for NGC 5044.

5.1.3 NGC 4649

Although CADET identified only the inner cavity generation, β -modelling revealed the second generation about 20 kiloparsecs from the centre. The second generation was revealed only by β -modelling. The north-eastern cavity in the second generation is surrounded by a brighter rim. Deeper *Chandra* observations would greatly help with the confirmation of the second generation.

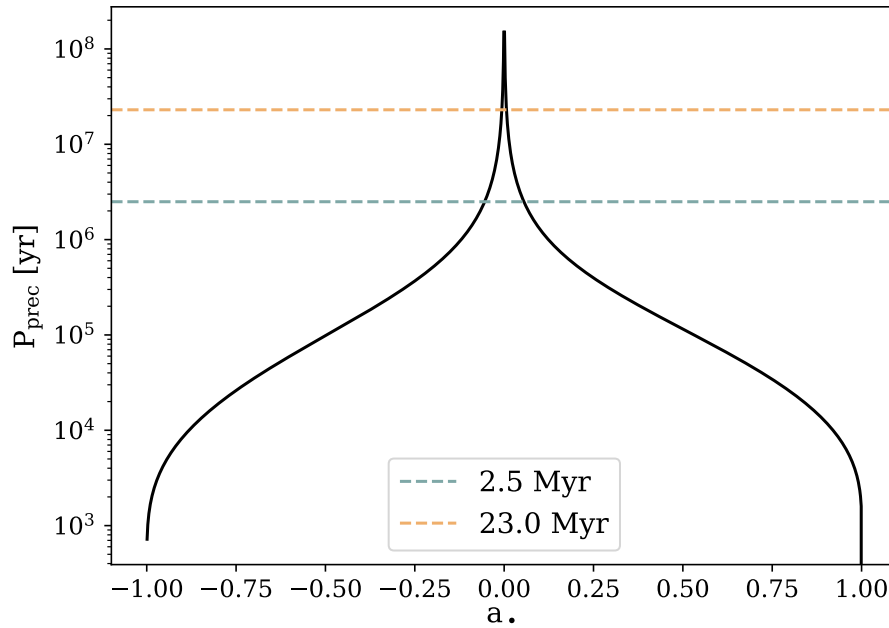


Figure 5.4: Precession period in the case of Lense-Thirring precession of an accretion disc as a function of its rotational parameter a_* . Dashed lines represent the precession periods derived for NGC 5044.

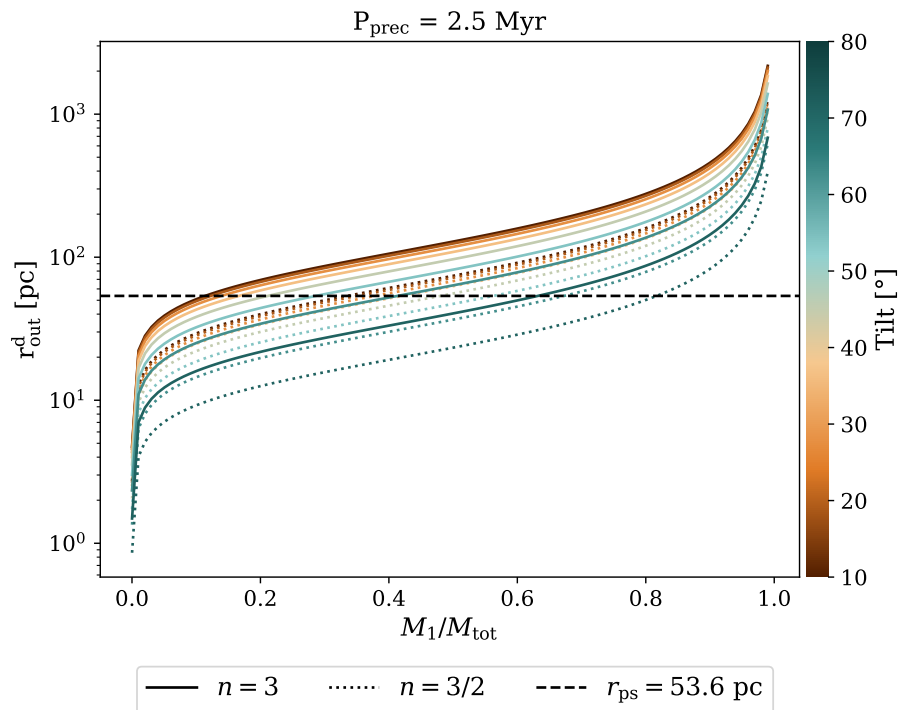


Figure 5.5: The extent of the outer processing disc as a function of the primary's mass fraction.

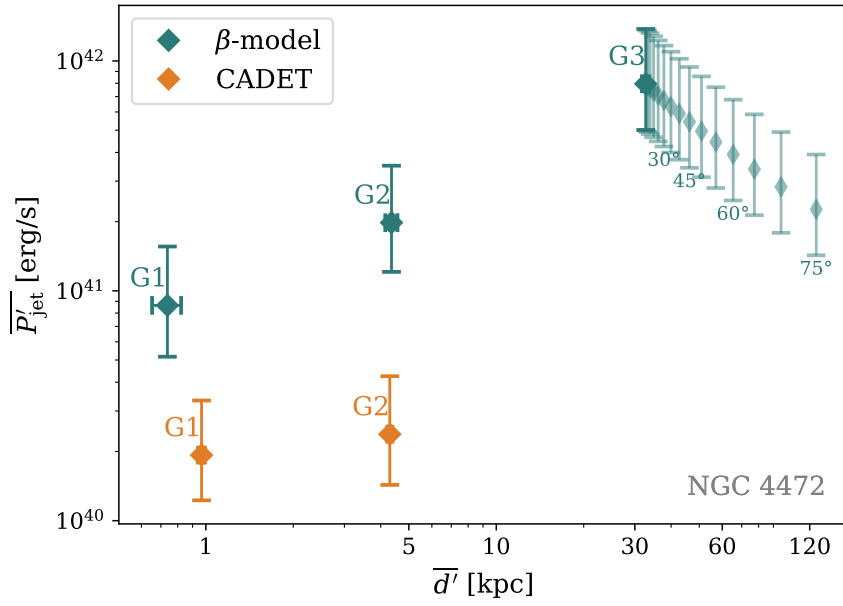


Figure 5.6: Projected cumulative jet powers $\overline{P'_{\text{jet}}}$ versus the average projected cavity generation distance $\overline{d'}$ for NGC 4472. For the G1 and G2 generations, inclination was not accounted for, it was rather assumed that $\overline{P'_{\text{jet}}} = \overline{P_{\text{jet}}}$. Recalculated intrinsic cumulative $\overline{P_{\text{jet}}}$ for the G3 generation from a presumed inclination are depicted by fainter data points.

5.1.4 NGC 4472

Although regions detected by both identification methods coincide well for NGC 4472, the soft band image hints at an oddly-shaped northwestern cavity. The peculiar shape is more pronounced in the β -model residual image. The detected regions seem to extend into a banana-shaped surface brightness depression that encloses central emission from the west. The most likely explanation seems to be that the cavity is inclined towards us and its eastern edge is overlapped by the central emission.

XMM-Newton image of NGC 4472 shows a slight surface brightness enhancement with a very subtle drop in the middle about 30 kiloparsecs from the centre of the galaxy in both eastern and south-western directions of the cavities. Kraft et al. (2011) identified the enhancements as arms of cool gas being pushed away by buoyantly rising bubbles. We decided to consider these subtle brightness depressions as the third cavity generation.

Fig. 4.12 shows that $\overline{P_{\text{jet}}}$ values determined for CADET cavities tend to follow a constant trend. However, adding the candidate third generation increased the time-averaged cycle-corrected jet power $\overline{P_{\text{jet}}}$. On the other hand, if we suppose the jet power of the third generation to be measured at some inclination, i.e., measuring its projected jet power $\overline{P'_{\text{jet}}}$ – and recalculating the intrinsic value, as is depicted in Fig. 5.6, the trend seemingly drops towards a constant value. If such inclination is indeed present, the cavities are much harder to detect due to the low contrast.

5.2 Toy model

We considered an oblate and a prolate cavity at a distance of 10 kpc from the centre of the galaxy. They were embedded in an isothermal atmosphere (with $T = 10^7$ K), in which the β -model describes both the electron density and the pressure profile. We chose a β -model that would describe a giant elliptical with the following parameters: $n_0 = 0.1 \text{ cm}^{-3}$, $r_c = 10 \text{ kpc}$, $\beta = 0.45$. The cavity shapes were chosen so that they had the same volume, with one being elongated along the galactocentric direction (a prolate cavity) and the other perpendicularly to the galactocentric direction (an oblate cavity). For clarity, their parameters are listed in Tab. 5.1.

Table 5.1: Properties of artificial cavities at distance $d = 10 \text{ kpc}$.

	τ	R_w [kpc]	R_l [kpc]
Oblate cavity	0.62	5.5	3.4
Prolate cavity	1.60	4	6.4

Then we inclined the system by letting the projected distance d' change according to Eq. 3.9 and the projected semi-axis in the galactocentric direction R_l' as described by Eq. 3.11. We imposed a cut-off in inclination angle at $i = 60^\circ$, at which we considered the cavity to be not that easily discernible due to low contrast.

For the new projected d' and R_l' , we calculated t'_{buo} , E'_{inj} and P'_{jet} that we would measure if the system were inclined by some inclination, i.e., the projected values. Our results are shown in Fig. 5.7.

Distance underestimation due to the inclination causes the pressure to be overestimated. Large inclination causes the projected buoyancy timescale t'_{buo} to be heavily underestimated for both cavity types. If the system is inclined by 50° , measured t'_{buo} represents only about 60% of the intrinsic value for a prolate cavity, but around 45% for an oblate cavity. As for the cavity's semi-axis in the galactocentric direction R_l' , and therefore its projected volume V' , it is always an overestimate for the oblate cavity but an underestimate for the prolate cavity. Injected energy follows the same trend; however, for the prolate cavity, the trend is more moderate. On the other hand, a factor of two uncertainty in this case seems to incorporate for projection effects affecting the injected energy.

For our purpose, jet powers are of the utmost interest. For the prolate cavity, the trend is subtle. For the projected P'_{jet} measured at 60° inclination, the intrinsic value would, in this particular case, just fall on the limit of the assumed factor-of-two uncertainty. Seemingly, oblate cavities are more prone to the projection effects affecting the measured P'_{jet} . If the cavity is inclined by 60° , intrinsic P_{jet} seems to be about 6 times smaller than the measured value P'_{jet} , as can be seen in the lower right part of Fig. 5.7.

Subsequently, we calculated a *relative jet power change* $\Delta P_{\text{jet}}^{\text{rel}}$ as

$$\Delta P_{\text{jet}}^{\text{rel}} = \frac{P'_{\text{jet}}(i) - P_{\text{jet}}(i = 0^\circ)}{P_{\text{jet}}(i = 0^\circ)}, \quad (5.1)$$

where $P'_{\text{jet}}(i)$ is the projected jet power measured at inclination i and $P_{\text{jet}}(i = 0^\circ)$ is the value measured if the system lies in the plane of the sky, for a variety of set-ups to prevent a biased cavity selection. Our results are depicted in Fig. 5.8.

For larger inclinations, the projected P_{jet} will always be overestimated, and in all cases, oblate cavities ($\tau < 1$) are more affected by projection effects. As shown in the left panel of Fig. 5.8, the relative change $\Delta P_{\text{jet}}^{\text{rel}}$ for a cavity presumed to be attached and expanding at the local speed of sound is not as significant as for buoyancy-driven cavities (middle and right panels). This is due to the shallower pressure profile closer to the galaxy and the fact that, while the buoyancy timescale depends both on the projected volume and distance, the sound-speed timescale is only a function of the distance.

Having modelled $\Delta P_{\text{jet}}^{\text{rel}}$ for various distances for buoyancy-driven cavities, we can say that cavity distance does not play a role in how overestimated the measured value is going to be for these cavities. On the other hand, the measured jet power of buoyantly rising cavities lying as far from the plane of the sky as 60° is going to be larger by an order of magnitude. Comparing the bottom panels in Fig. 5.8, it seems that cavity distance relative to the core radius r_c plays a substantial role in determining the amount of overestimation.

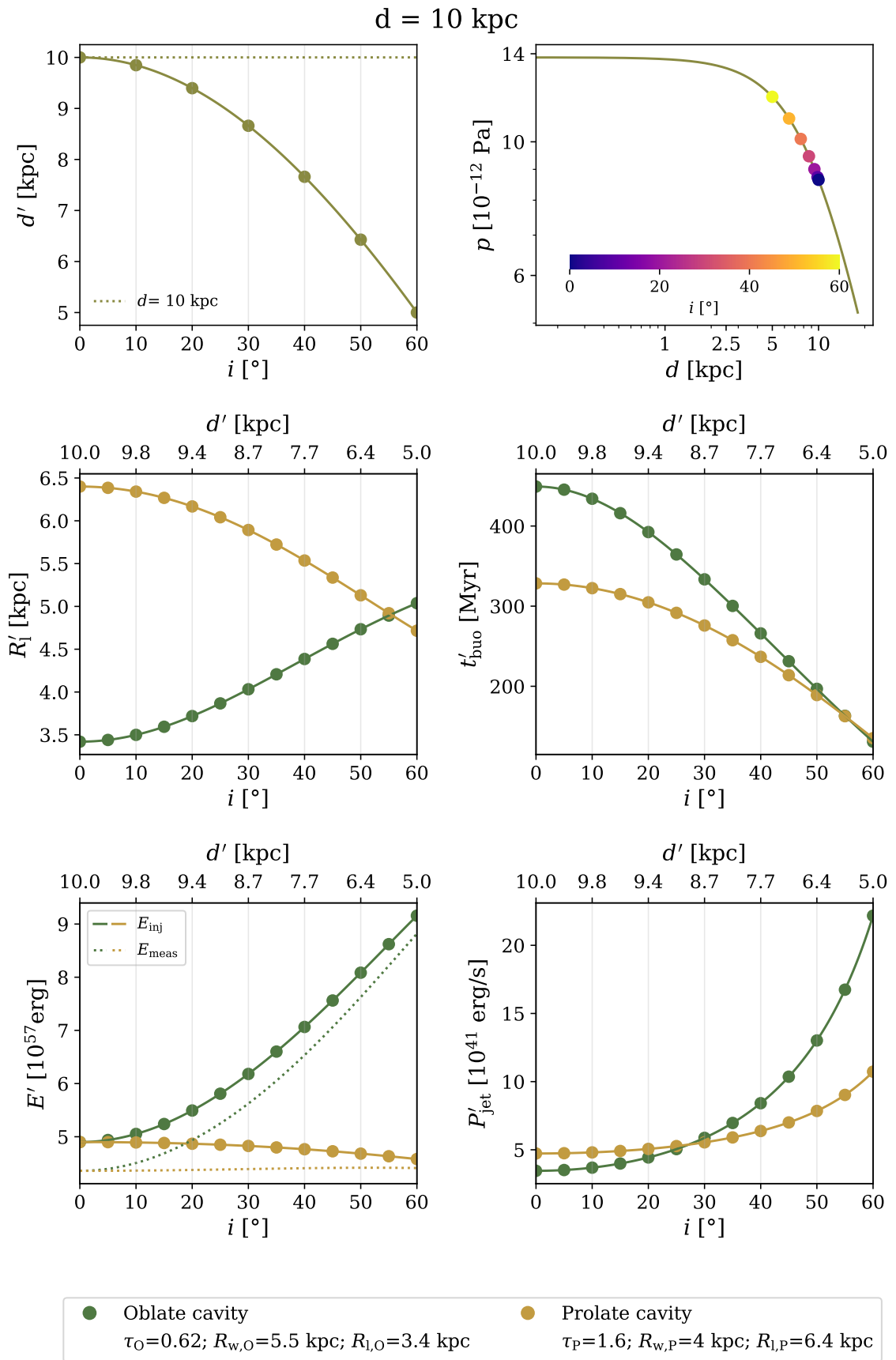


Figure 5.7: Results of modelling the inclination's effect on the cavity properties.

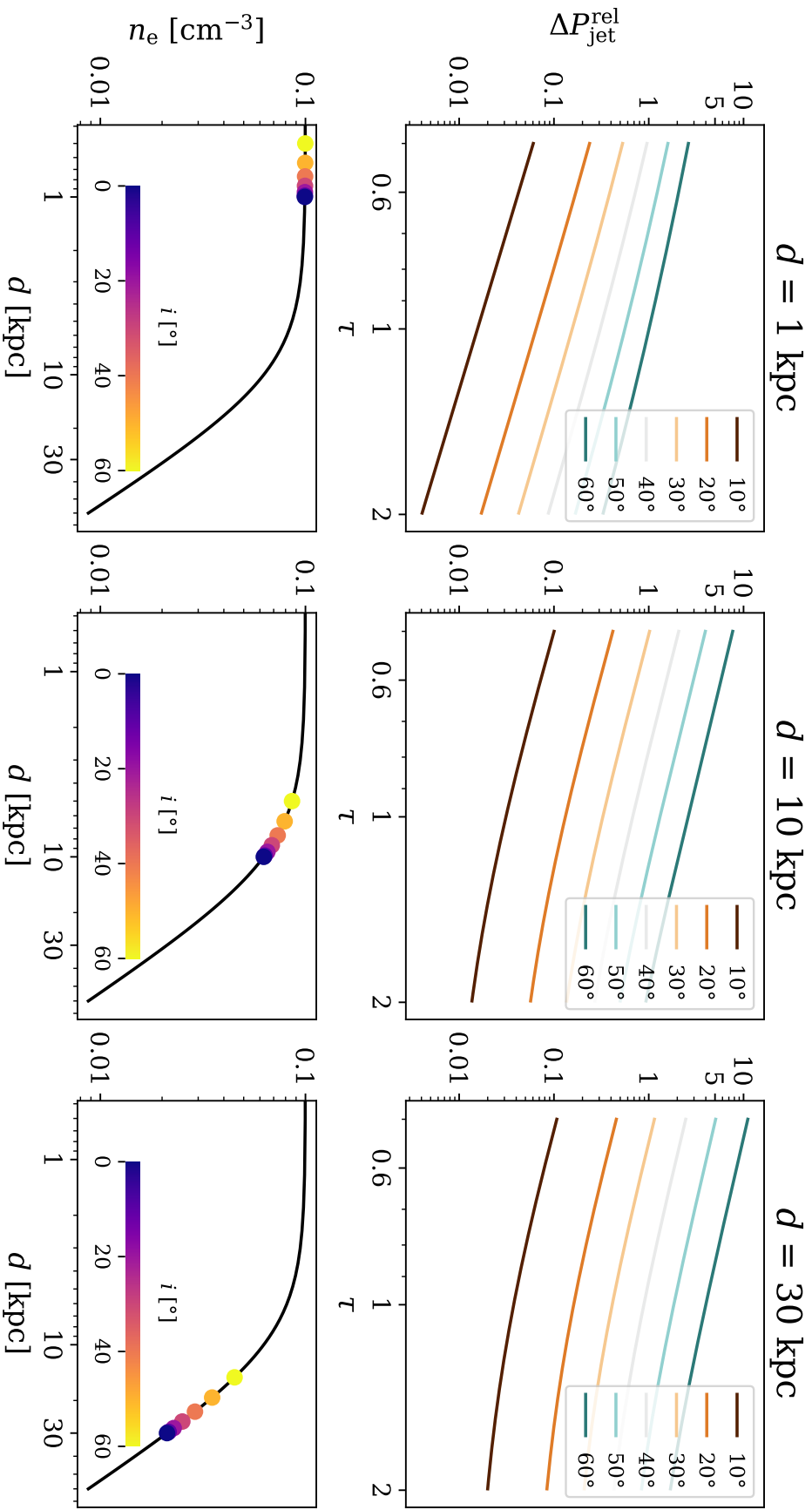


Figure 5.8: Top panels: Relative jet power changed $\Delta P_{\text{jet}}^{\text{rel}}$ for different cavities as a function of their intrinsic radial elongations τ . Bottom panels: β -model with denoted projected distances for each cavity. Left: A cavity at 1 kiloparsec, which is thought to be still attached and expanding at the speed of sound. Middle: A buoyancy-driven cavity at 10 kiloparsecs. Right: A buoyancy-driven cavity at 30 kiloparsecs.

Conclusion

In this thesis, we have devoted our endeavours to study radio-mechanical AGN feedback in four nearby giant elliptical galaxies harbouring hot atmospheres: NGC 5813, NGC 5044, NGC 4649 and NGC 4472. All of the systems are known to showcase multiple generations of X-ray cavities, thus hinting at the history of AGN feedback.

We carried out spectral analysis to obtain deprojected radial profiles for temperature and electron density of the hot atmospheres around each source. Image analysis was performed to reveal the positions and extent of individual cavities. For cavity identification, we opted for two different methods: a classical β -model subtraction combined with visual cavity detection and a novel machine-learning pipeline, CADET.

For every cavity, we calculated cavity timescales and the energy associated with the cavities. In these calculations, we opted for slightly different methods than are usually deployed in the literature. For the age of an attached cavity, the sound-speed timescale was considered to be the best estimate, while the cavity age for a detached cavity was considered its buoyancy timescale corrected by the age of the previous cavity if the system is aligned. For the injected energy, which is typically considered to be the cavity's enthalpy, we also incorporated an estimate of energy already deposited into the surrounding medium. The cavities that detached from the jet much sooner, and, therefore, were much older, were affected by the improved methodology more than the inner, i.e., younger cavities.

The ultimate goal of this work was to probe the consistency of jet power across the whole duty cycle of the central AGN. We can conclude that for nicely aligned systems, e.g., NGC 5813 – Fig. 4.3 and NGC 4649 – Fig. 4.9, the cumulative jet power per generation tends to oscillate around a cycle-corrected time-averaged value of jet power, although for NGC 4649, a third cavity generation would be appreciated to prove this theory. On the other hand, in a misaligned system of cavities in NGC 5044, the outer aligned cavity generation did not conform to our prediction, as is depicted in Fig. 4.6. As we mentioned in Chapter 5, projection effects are a plausible reason for the overestimated jet power in our measurements (5.2). Adding a potential third generation to the dataset for NGC 4472 also did not cause the jet power values to follow a constant value. The difference was not as significant if we presumed the generation to be inclined by an angle larger than 50° (Fig. 5.6).

Various precession models were examined to explain the plausibility of precession causing large misalignments in the NGC 5044. A precession caused by a secondary BH was ruled out based on the resulting parameters of the precession, such as the separation of BBH constituents and the precessing disc extent. Lense-Thirring preces-

sion seems to be a plausible precession mechanism, but the calculations, especially for Lense-Thirring precession, would need some further fine-tuning.

Lastly, we modelled the inclination's effect on the measured values connected with cavities, especially the power of the jet excavating it. We found that for oblate cavities, the inclination heavily skews our measurements. If the cavity is still attached, the inclination, although playing a role, will not affect the values as much as in the case of a buoyant bubble further from the centre.

Appendix

A Observations

Table A.1: Used OBSIDs.

Galaxy	OBSID	Instrument	Date [yyyy-mm-dd]	Exposure [ks]
NGC 5813	5907 †	ACIS-S	2005-04-02	48.4
	9517 †	ACIS-S	2008-06-05	98.8
	11329 †	ACIS-S	2011-06-06	10.0
	12951	ACIS-S	2011-03-28	74.0
	12952	ACIS-S	2011-04-05	143.1
	12953	ACIS-S	2011-04-07	31.8
	13246	ACIS-S	2011-03-30	45.0
	13247	ACIS-S	2011-03-31	35.8
	13253	ACIS-S	2011-04-08	118.0
	13255	ACIS-S	2011-04-10	43.4
NGC 5044	798	ACIS-S	2000-03-19	20.5
	9399	ACIS-S	2008-03-07	82.7
	17195	ACIS-S	2015-06-06	78.0
	17196	ACIS-S	2015-05-11	88.9
	17653	ACIS-S	2015-05-07	35.5
	17654	ACIS-S	2015-05-10	25.0
	17666	ACIS-S	2015-08-23	88.6
NGC 4649	785 †	ACIS-S	2000-04-20	38.1
	8182	ACIS-S	2007-01-30	52.4
	8507	ACIS-S	2007-02-01	17.5
	12975	ACIS-S	2011-08-08	84.9
	12976	ACIS-S	2011-02-24	101.0
	14328	ACIS-S	2011-08-12	14.0

Table A.1 – *to be continued.*

Table A.1 – *continued.*

Galaxy	OBSID	Instrument	Date [yyyy-mm-dd]	Exposure [ks]
NGC 4472	321 †	ACIS-S	2000-06-12	39.6
	322 †	ACIS-I	2000-03-19	10.4
	8095	ACIS-S	2008-02-23	5.1
	8107 †	ACIS-S	2007-04-28	5.1
	11274	ACIS-S	2010-02-27	39.7
	12888	ACIS-S	2011-02-21	159.3
	12889	ACIS-S	2011-02-14	135.6
	12978	ACIS-S	2010-11-20	19.8
	15757	ACIS-I	2014-04-18	29.7
	16260	ACIS-S	2014-08-04	24.7
	16261	ACIS-S	2015-02-24	22.8
	16262	ACIS-S	2016-04-30	24.7
	21647	ACIS-S	2019-04-17	29.7
	21648	ACIS-S	2020-04-09	29.7
	21649	ACIS-S	2021-03-02	19.8
	24981	ACIS-S	2021-03-08	11.5

† Not used for spectral analysis.

B Cavity timescales and energetics

B.1 NGC 5813

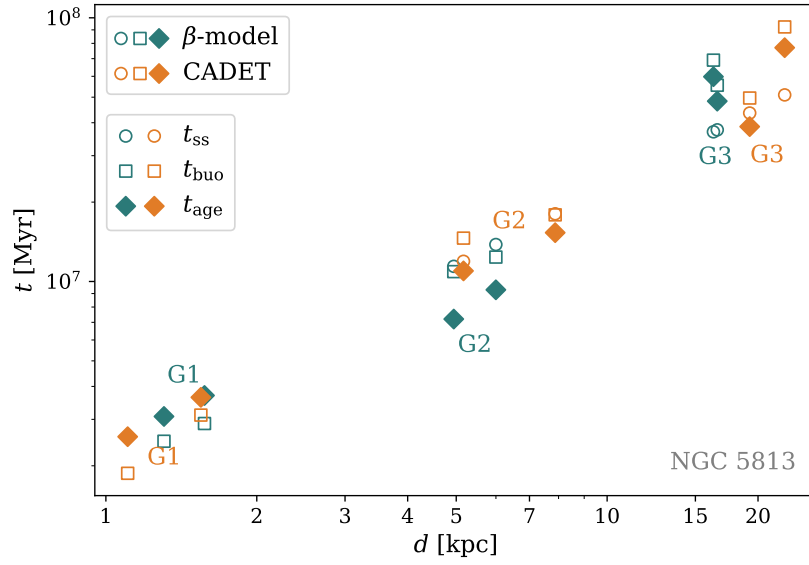


Figure B.1: Corrected cavity ages t_{age} compared to the usual approach of calculating cavity timescales t_{ss} , t_{buo} .

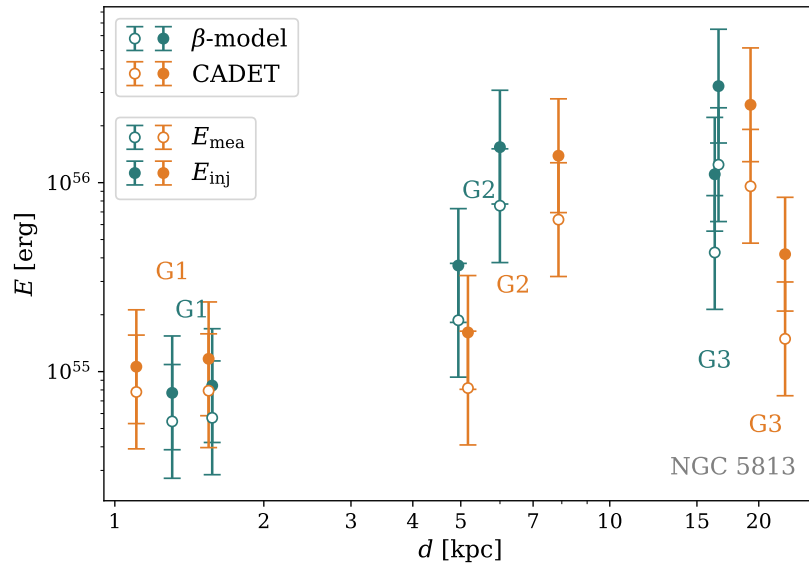


Figure B.2: Measured cavity energy E_{mea} and injected energy E_{inj} as a function of cavity distance d .

B.2 NGC 5044

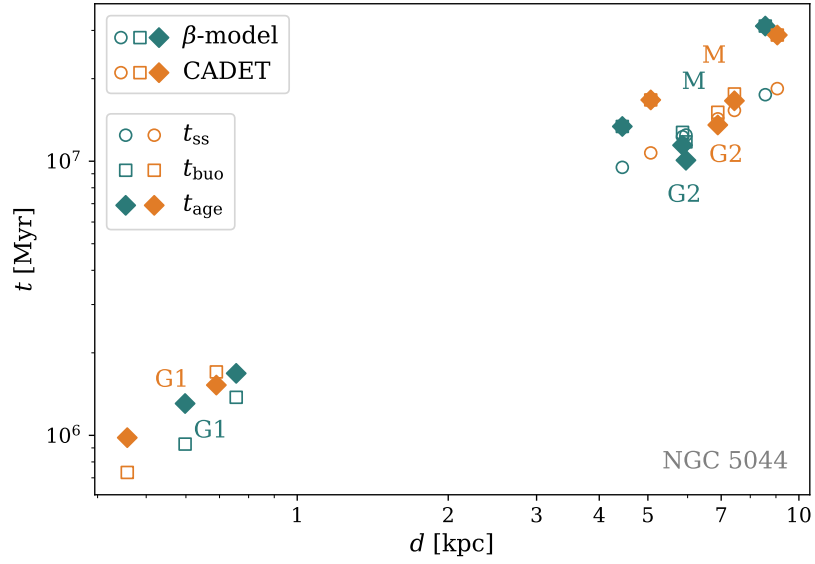


Figure B.3: Corrected cavity ages t_{age} compared to usual approach of calculating t_{ss} , t_{buo} for cavities.

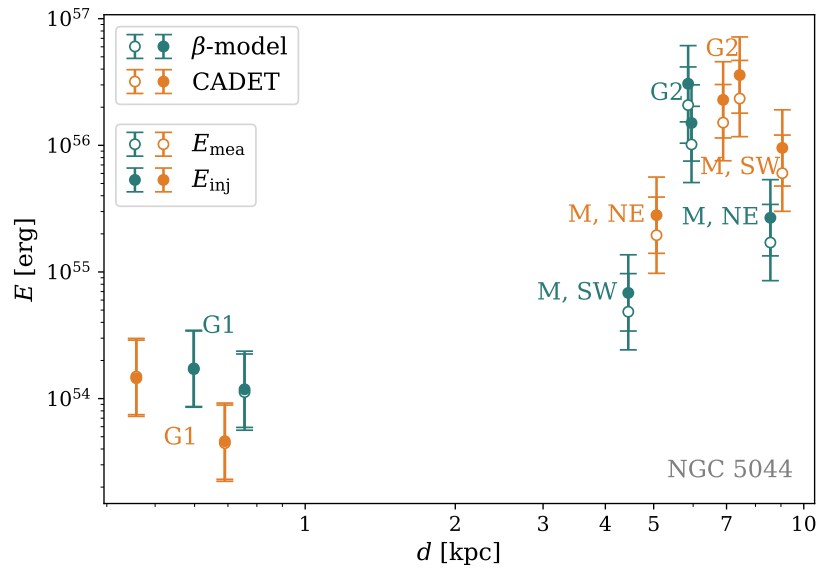


Figure B.4: Injected energy E_{inj} , compared with measured energy E_{mea} , as a function of average distance of cavities \bar{d} .

B.3 NGC 4649

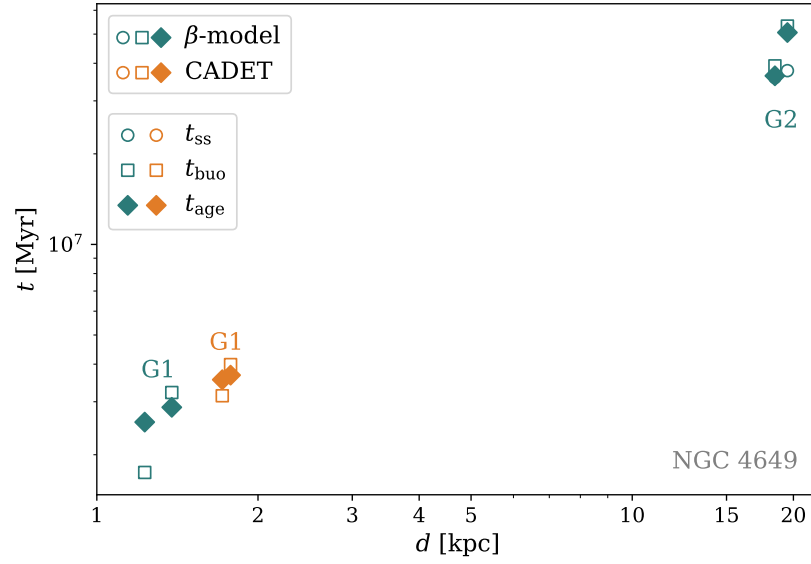


Figure B.5: Corrected cavity ages t_{age} and timescales t_{ss} , t_{buo} as a function of cavity distance d .

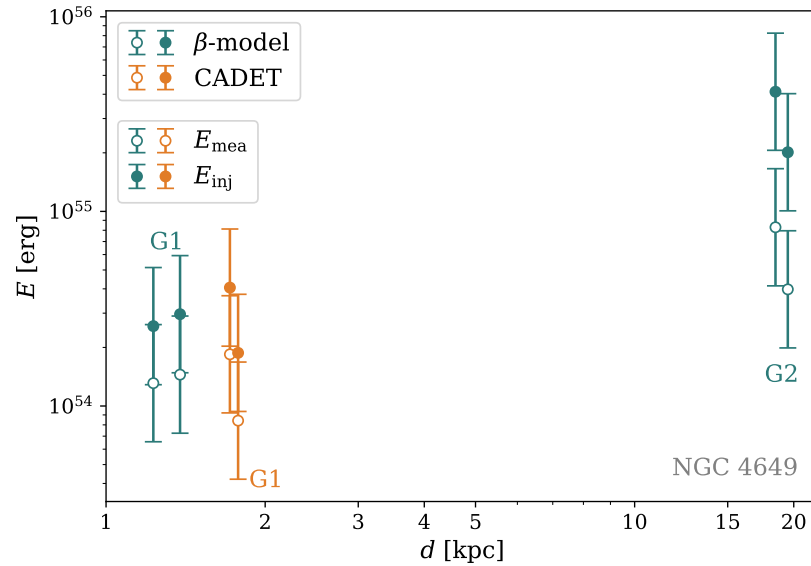


Figure B.6: Injected and measured energy, E_{inj} and E_{mea} , respectively, as a function of cavity distance d .

B.4 NGC 4472

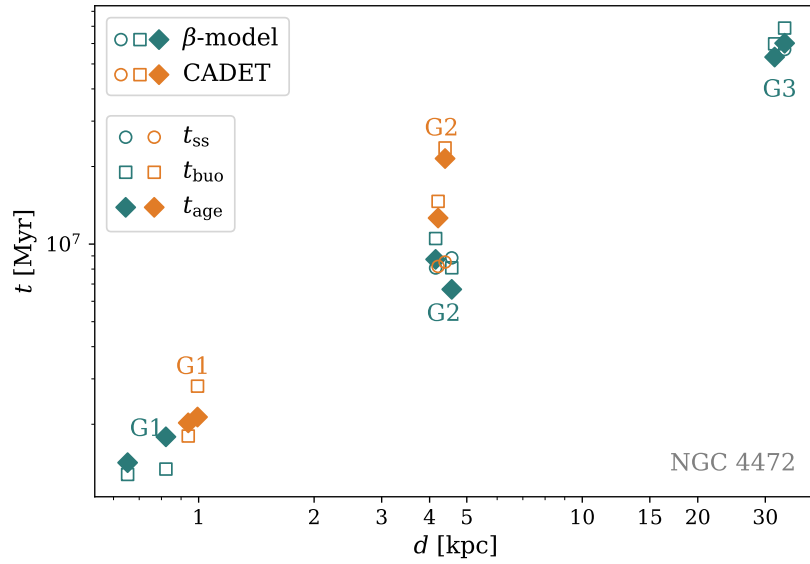


Figure B.7: Corrected cavity ages t_{age} and timescales t_{ss} , t_{buo} as a function of cavity distance d .

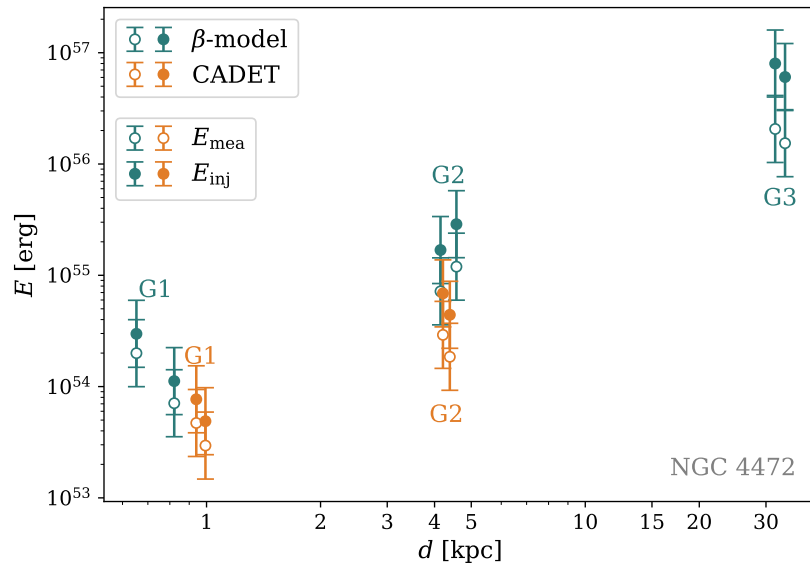


Figure B.8: Injected and measured energy, E_{inj} and E_{mea} , respectively, as a function of cavity distance d .

C Eddington efficiency

Although Fig. 5.3 shows the Lense-Thirring precession of a single BH as a function of the Eddington efficiency ϵ , Eq. 3.12 requires the black hole's accretion rate \dot{M}_\bullet . For clarity, we now present the approach used in our calculations.

Firstly, we assumed that the SMBH accretes at $\epsilon \approx 10^{-4} - 10^{-2}$ (taken from Hlavacek-Larrondo et al., 2022). Eddington accretion rate \dot{M}_{Edd} was calculated as

$$\dot{M}_{\text{Edd}} = \frac{L_{\text{Edd}}}{\eta c^2}, \quad (\text{C.1})$$

where η is the conversion factor (assumed $\eta \sim 0.1$) and c is the speed of light (Binney and Merrifield, 1998). Eddington luminosity L_{Edd} was approximated as

$$L_{\text{Edd}} \doteq 1.26 \cdot 10^{38} \left(\frac{M_\bullet}{M_\odot} \right) \text{ erg/s} \quad (\text{C.2})$$

(Schneider, 2006). The mass of the SMBH was taken from the literature⁴ or alternatively, it could be calculated from the following $M - \sigma$ relation, e.g.:

$$M_\bullet = 1.3 \cdot 10^8 M_\odot \left(\frac{\sigma_v}{200 \text{ km/s}} \right)^{4.72} \quad (\text{C.3})$$

(Merritt and Ferrarese, 2001).

Accretion rate \dot{M}_\bullet was calculated as

$$\dot{M}_\bullet = \epsilon \dot{M}_{\text{Edd}} \quad (\text{C.4})$$

D Understanding the amount of jet power

When thinking about how to illustrate the above-mentioned amounts of energy released by AGN jets to my friends, I tried to come up with some easy-to-digest comparisons. For example, the most powerful engine used in F1 Grand Prix race was BMW M12/13⁵, which produced around 1000 horsepower during a race, which corresponds to about $\sim 10^{13}$ erg/s. In comparison with the average jet power in our sample of cavities (about $\sim 10^{40}$ erg/s), you would need 10^{27} of these engines to have the same energy output. If you consider thermal energy produced by a Super heavy booster with 33 Raptor engines, it amounts to about 10^{18} erg/s. Thus, you would need a modest amount of 10^{22} of these boosters. If you were to compare it to total energy consumption of the whole Earth ($\sim 4 \cdot 10^{20}$ J/yr⁶), you would need around 10^{20} Earths.

⁴See the last row of Tab. 3.1.

⁵Engine Builder Magazine (2015).

⁶International Energy Agency's report (2019).

References

- S. W. Allen, R. J. H. Dunn, A. C. Fabian, G. B. Taylor, and C. S. Reynolds. The relation between accretion rate and jet power in X-ray luminous elliptical galaxies. , 372(1): 21–30, Oct. 2006. doi: 10.1111/j.1365-2966.2006.10778.x.
- M. E. Anderson and R. Sunyaev. FUV line emission, gas kinematics, and discovery of [Fe XXI] λ 1354.1 in the sightline toward a filament in M87. , 617:A123, Oct. 2018. doi: 10.1051/0004-6361/201732510.
- K. A. Arnaud. XSPEC: The First Ten Years. In G. H. Jacoby and J. Barnes, editors, *Astronomical Data Analysis Software and Systems V*, volume 101 of *Astronomical Society of the Pacific Conference Series*, page 17, Jan. 1996.
- M. Balucinska-Church and D. McCammon. Photoelectric Absorption Cross Sections with Variable Abundances. , 400:699, Dec. 1992. doi: 10.1086/172032.
- J. Binney and M. Merrifield. *Galactic Astronomy*. 1998.
- L. Bîrzan, D. A. Rafferty, B. R. McNamara, M. W. Wise, and P. E. J. Nulsen. A Systematic Study of Radio-induced X-Ray Cavities in Clusters, Groups, and Galaxies. , 607(2): 800–809, June 2004. doi: 10.1086/383519.
- H. Boehringer, W. Voges, A. C. Fabian, A. C. Edge, and D. M. Neumann. A ROSAT HRI study of the interaction of the X-ray emitting gas and radio lobes of NGC 1275. , 264: L25–L28, Oct. 1993. doi: 10.1093/mnras/264.1.L25.
- H. Bondi. On spherically symmetrical accretion. , 112:195, Jan. 1952. doi: 10.1093/mnras/112.2.195.
- S. Britzen, C. Fendt, G. Witzel, S. J. Qian, I. N. Pashchenko, O. Kurtanidze, M. Zajacek, G. Martinez, V. Karas, M. Aller, H. Aller, A. Eckart, K. Nilsson, P. Arévalo, J. Cuadra, M. Subroweit, and A. Witzel. OJ287: deciphering the ‘Rosetta stone of blazars. , 478 (3):3199–3219, Aug. 2018. doi: 10.1093/mnras/sty1026.
- M. Brüggen, E. Scannapieco, and S. Heinz. Evolution of X-ray cavities. , 395(4):2210–2220, June 2009. doi: 10.1111/j.1365-2966.2009.14684.x.
- J. O. Burns, E. J. Hallman, B. Gantner, P. M. Motl, and M. L. Norman. Why Do Only Some Galaxy Clusters Have Cool Cores? , 675(2):1125–1140, Mar. 2008. doi: 10.1086/526514.

- A. Caproni, H. J. Mosquera Cuesta, and Z. Abraham. Observational Evidence of Spin-induced Precession in Active Galactic Nuclei. , 616(2):L99–L102, Dec. 2004. doi: 10.1086/426863.
- A. Cavaliere and R. Fusco-Femiano. X-rays from hot plasma in clusters of galaxies. , 49: 137–144, May 1976.
- E. Churazov, R. Sunyaev, W. Forman, and H. Böhringer. Cooling flows as a calorimeter of active galactic nucleus mechanical power. , 332(3):729–734, May 2002. doi: 10.1046/j.1365-8711.2002.05332.x.
- S. Diehl, H. Li, C. L. Fryer, and D. Rafferty. Constraining the Nature of X-Ray Cavities in Clusters and Galaxies. , 687(1):173–192, Nov. 2008. doi: 10.1086/591310.
- R. Dong, J. Rasmussen, and J. S. Mulchaey. A Systematic Search for X-ray Cavities in the Hot Gas of Galaxy Groups. , 712(2):883–900, Apr. 2010. doi: 10.1088/0004-637X/712/2/883.
- S. Ettori. β -model and cooling flows in X-ray clusters of galaxies. , 318(4):1041–1046, Nov. 2000. doi: 10.1046/j.1365-8711.2000.03664.x.
- A. C. Fabian. Cooling Flows in Clusters of Galaxies. , 32:277–318, Jan. 1994. doi: 10.1146/annurev.aa.32.090194.001425.
- A. C. Fabian. Observational Evidence of Active Galactic Nuclei Feedback. , 50:455–489, Sept. 2012. doi: 10.1146/annurev-astro-081811-125521.
- A. C. Fabian, E. M. Hu, L. L. Cowie, and J. Grindlay. The distribution and morphology of X-ray emitting gas in the core of the Perseus cluster. , 248:47–54, Aug. 1981. doi: 10.1086/159128.
- W. Forman, E. Kellogg, H. Gursky, H. Tananbaum, and R. Giacconi. Observations of the Extended X-Ray Sources in the Perseus and Coma Clusters from UHURU. , 178: 309–316, Dec. 1972. doi: 10.1086/151791.
- W. Forman, J. Schwarz, C. Jones, W. Liller, and A. C. Fabian. X-ray observations of galaxies in the Virgo cluster. , 234:L27–L31, Nov. 1979. doi: 10.1086/183103.
- W. Forman, C. Jones, and W. Tucker. Hot Coronae around Early-Type Galaxies. , 293: 102, June 1985. doi: 10.1086/163218.
- A. Fruscione, J. C. McDowell, G. E. Allen, N. S. Brickhouse, D. J. Burke, J. E. Davis, N. Durham, M. Elvis, E. C. Galle, D. E. Harris, D. P. Huenemoerder, J. C. Houck, B. Ishibashi, M. Karovska, F. Nicastro, M. S. Noble, M. A. Nowak, F. A. Primini, A. Siemiginowska, R. K. Smith, and M. Wise. CIAO: Chandra’s data analysis system. In D. R. Silva and R. E. Doxsey, editors, *Observatory Operations: Strategies, Processes, and Systems*, volume 6270 of *Society of Photo-Optical Instrumentation Engineers (SPIE) Conference Series*, page 62701V, June 2006. doi: 10.1117/12.671760.

- M. Gaspari, M. Ruszkowski, and S. P. Oh. Chaotic cold accretion on to black holes. , 432 (4):3401–3422, July 2013. doi: 10.1093/mnras/stt692.
- S. Giacintucci, E. O’Sullivan, J. Vrtilik, L. P. David, S. Raychaudhury, T. Venturi, R. M. Athreya, T. E. Clarke, M. Murgia, P. Mazzotta, M. Gitti, T. Ponman, C. H. Ishwara-Chandra, C. Jones, and W. R. Forman. A combined low-radio frequency/x-ray study of galaxy groups. i. giant metrewave radio telescope observations at 235 mhz and 610 mhz. *The Astrophysical Journal*, 732(2):95, apr 2011. doi: 10.1088/0004-637X/732/2/95. URL <https://dx.doi.org/10.1088/0004-637X/732/2/95>.
- F. Guo. The Shape of X-Ray Cavities in Galaxy Clusters: Probing Jet Properties and Viscosity. , 803(1):48, Apr. 2015. doi: 10.1088/0004-637X/803/1/48.
- F. Guo. Probing the Physics of Mechanical AGN Feedback with Radial Elongations of X-Ray Cavities. , 903(1):3, Nov. 2020. doi: 10.3847/1538-4357/abb777.
- H. Gursky, E. Kellogg, S. Murray, C. Leong, H. Tananbaum, and R. Giacconi. A Strong X-Ray Source in the Coma Cluster Observed by UHURU. , 167:L81, Aug. 1971. doi: 10.1086/180765.
- J. Hlavacek-Larrondo, Y. Li, and E. Churazov. AGN Feedback in Groups and Clusters of Galaxies. In C. Bambi and A. Sanganello, editors, *Handbook of X-ray and Gamma-ray Astrophysics*, page 5. 2022. doi: 10.1007/978-981-16-4544-0_122-1.
- D. S. Hudson, R. Mittal, T. H. Reiprich, P. E. J. Nulsen, H. Andernach, and C. L. Sarazin. What is a cool-core cluster? a detailed analysis of the cores of the X-ray flux-limited HIFLUGCS cluster sample. , 513:A37, Apr. 2010. doi: 10.1051/0004-6361/200912377.
- J. Kormendy and L. C. Ho. Coevolution (Or Not) of Supermassive Black Holes and Host Galaxies. , 51(1):511–653, Aug. 2013. doi: 10.1146/annurev-astro-082708-101811.
- R. P. Kraft, W. R. Forman, C. Jones, P. E. J. Nulsen, M. J. Hardcastle, S. Raychaudhury, D. A. Evans, G. R. Sivakoff, and C. L. Sarazin. The Gas Dynamics of NGC 4472 Revealed by XMM-Newton. , 727(1):41, Jan. 2011. doi: 10.1088/0004-637X/727/1/41.
- K. Lakhchaura, N. Werner, M. Sun, R. E. A. Canning, M. Gaspari, S. W. Allen, T. Connor, M. Donahue, and C. Sarazin. Thermodynamic properties, multiphase gas, and AGN feedback in a large sample of giant ellipticals. , 481(4):4472–4504, Dec. 2018. doi: 10.1093/mnras/sty2565.
- J. D. Larwood. The tidal disruption of protoplanetary accretion discs. *Monthly Notices of the Royal Astronomical Society*, 290(3):490–504, 09 1997. ISSN 0035-8711. doi: 10.1093/mnras/290.3.490. URL <https://doi.org/10.1093/mnras/290.3.490>.
- K. Lodders, H. Palme, and H. P. Gail. Abundances of the Elements in the Solar System. *Landolt Börnstein*, 4B:712, Jan. 2009. doi: 10.1007/978-3-540-88055-4_34.
- Lu Ju-fu. -disks and the precession of extragalactic jets. *Chinese Astronomy and Astrophysics*, 16(2):133–136, 1992. ISSN 0275-1062. doi: <https://doi.org/10.1093/mnras/sty2565>.

- 1016/0275-1062(92)90095-S. URL <https://www.sciencedirect.com/science/article/pii/027510629290095S>.
- D. Makarov, P. Prugniel, N. Terekhova, H. Courtois, and I. Vauglin. HyperLEDA. III. The catalogue of extragalactic distances. , 570:A13, Oct. 2014. doi: 10.1051/0004-6361/201423496.
- W. G. Mathews and F. Brighenti. Hot Gas in and around Elliptical Galaxies. , 41:191–239, Jan. 2003. doi: 10.1146/annurev.astro.41.090401.094542.
- W. G. Mathews, A. Faltenbacher, and F. Brighenti. Heating cooling flows with weak shock waves. *The Astrophysical Journal*, 638(2):659, feb 2006. doi: 10.1086/499119. URL <https://dx.doi.org/10.1086/499119>.
- B. R. McNamara and P. E. J. Nulsen. Heating Hot Atmospheres with Active Galactic Nuclei. , 45(1):117–175, Sept. 2007. doi: 10.1146/annurev.astro.45.051806.110625.
- D. Merritt and L. Ferrarese. The m_{\bullet} - relation for supermassive black holes. *The Astrophysical Journal*, 547(1):140, jan 2001. doi: 10.1086/318372. URL <https://dx.doi.org/10.1086/318372>.
- R. Narayan and I. Yi. Advection-dominated Accretion: A Self-similar Solution. , 428:L13, June 1994. doi: 10.1086/187381.
- E. O’Sullivan, F. Combes, P. Salomé, L. P. David, A. Babul, J. M. Vrtilik, J. Lim, V. Olivares, S. Raychaudhury, and G. Schellenberger. Cold gas in a complete sample of group-dominant early-type galaxies. , 618:A126, Oct. 2018. doi: 10.1051/0004-6361/201833580.
- J. C. B. Papaloizou and C. Terquem. On the dynamics of tilted discs around young stars. *Monthly Notices of the Royal Astronomical Society*, 274(4):987–1001, 06 1995. ISSN 0035-8711. doi: 10.1093/mnras/274.4.987. URL <https://doi.org/10.1093/mnras/274.4.987>.
- J. R. Peterson and A. C. Fabian. X-ray spectroscopy of cooling clusters. , 427(1):1–39, Apr. 2006. doi: 10.1016/j.physrep.2005.12.007.
- J. R. Peterson, F. B. S. Paerels, J. S. Kaastra, M. Arnaud, T. H. Reiprich, A. C. Fabian, R. F. Mushotzky, J. G. Jernigan, and I. Sakelliou. X-ray imaging-spectroscopy of Abell 1835. , 365:L104–L109, Jan. 2001. doi: 10.1051/0004-6361:20000021.
- F. Pizzolato and N. Soker. On the Nature of Feedback Heating in Cooling Flow Clusters. , 632(2):821–830, Oct. 2005. doi: 10.1086/444344.
- T. Plšek, N. Werner, R. Grossová, M. Topinka, A. Simionescu, and S. W. Allen. The relation between accretion rate and jet power in early-type galaxies with thermally unstable hot atmospheres. , 517(3):3682–3710, Dec. 2022. doi: 10.1093/mnras/stac2770.

- T. Plšek, N. Werner, M. Topinka, and A. Simionescu. CAVITY DETECTION TOOL (CADET): Pipeline for detection of X-ray cavities in hot galactic and cluster atmospheres. , Nov. 2023. doi: 10.1093/mnras/stad3371.
- D. A. Rafferty, B. R. McNamara, P. E. J. Nulsen, and M. W. Wise. The feedback-regulated growth of black holes and bulges through gas accretion and starbursts in cluster central dominant galaxies. *The Astrophysical Journal*, 652(1):216, nov 2006. doi: 10.1086/507672. URL <https://dx.doi.org/10.1086/507672>.
- S. W. Randall, P. E. J. Nulsen, C. Jones, W. R. Forman, E. Bulbul, T. E. Clarke, R. Kraft, E. L. Blanton, L. David, N. Werner, M. Sun, M. Donahue, S. Giacintucci, and A. Simionescu. A Very Deep Chandra Observation of the Galaxy Group NGC 5813: AGN Shocks, Feedback, and Outburst History. , 805(2):112, June 2015. doi: 10.1088/0004-637X/805/2/112.
- R. P. Saglia, M. Opitsch, P. Erwin, J. Thomas, A. Beifiori, M. Fabricius, X. Mazzalay, N. Nowak, S. P. Rusli, and R. Bender. The sinfoni black hole survey: The black hole fundamental plane revisited and the paths of (co)evolution of supermassive black holes and bulges. *The Astrophysical Journal*, 818(1):47, feb 2016. doi: 10.3847/0004-637X/818/1/47. URL <https://dx.doi.org/10.3847/0004-637X/818/1/47>.
- J. S. Sanders, A. C. Fabian, S. W. Allen, R. G. Morris, J. Graham, and R. M. Johnstone. Cool X-ray emitting gas in the core of the Centaurus cluster of galaxies. , 385(3):1186–1200, Apr. 2008. doi: 10.1111/j.1365-2966.2008.12952.x.
- G. Schellenberger, L. P. David, J. Vrtilek, E. O’Sullivan, S. Giacintucci, W. Forman, C. Jones, and T. Venturi. A New Feedback Cycle in the Archetypal Cooling Flow Group NGC 5044. , 906(1):16, Jan. 2021. doi: 10.3847/1538-4357/abc488.
- P. Schneider. *Extragalactic Astronomy and Cosmology*. 2006.
- E. J. Schreier, P. Gorenstein, and E. D. Feigelson. High-resolution X-ray observations of M87 - Nucleus, jet and radio halo. , 261:42–50, Oct. 1982. doi: 10.1086/160316.
- J. Shin, J.-H. Woo, and J. S. Mulchaey. A Systematic Search for X-Ray Cavities in Galaxy Clusters, Groups, and Elliptical Galaxies. , 227(2):31, Dec. 2016. doi: 10.3847/1538-4365/227/2/31.
- W. B. Sparks, J. E. Pringle, R. F. Carswell, M. Donahue, R. Martin, M. Voit, M. Cracraft, N. Manset, and J. H. Hough. Hundred Thousand Degree Gas in the Virgo Cluster of Galaxies. , 750(1):L5, May 2012. doi: 10.1088/2041-8205/750/1/L5.
- F. Ubertosi, M. Gitti, F. Brighenti, G. Brunetti, M. McDonald, P. Nulsen, B. McNamara, S. Randall, W. Forman, M. Donahue, A. Ignesti, M. Gaspari, S. Etori, L. Feretti, E. L. Blanton, C. Jones, and M. Calzadilla. The Deepest Chandra View of RBS 797: Evidence for Two Pairs of Equidistant X-ray Cavities. , 923(2):L25, Dec. 2021. doi: 10.3847/2041-8213/ac374c.

- F. Ubertosi, G. Schellenberger, E. O'Sullivan, J. Vrtilek, S. Giacintucci, L. P. David, W. Forman, M. Gitti, T. Venturi, C. Jones, and F. Brighenti. Jet Reorientation in Central Galaxies of Clusters and Groups: Insights from VLBA and Chandra Data. , 961(1):134, Jan. 2024. doi: 10.3847/1538-4357/ad11d8.
- N. Werner, J. B. R. Oonk, R. E. A. Canning, S. W. Allen, A. Simionescu, J. Kos, R. J. van Weeren, A. C. Edge, A. C. Fabian, A. von der Linden, P. E. J. Nulsen, C. S. Reynolds, and M. Ruszkowski. The Nature of Filamentary Cold Gas in the Core of the Virgo Cluster. , 767(2):153, Apr. 2013. doi: 10.1088/0004-637X/767/2/153.
- N. Werner, J. B. R. Oonk, M. Sun, P. E. J. Nulsen, S. W. Allen, R. E. A. Canning, A. Simionescu, A. Hoffer, T. Connor, M. Donahue, A. C. Edge, A. C. Fabian, A. von der Linden, C. S. Reynolds, and M. Ruszkowski. The origin of cold gas in giant elliptical galaxies and its role in fuelling radio-mode AGN feedback. , 439(3):2291–2306, Apr. 2014. doi: 10.1093/mnras/stu006.
- N. Werner, B. R. McNamara, E. Churazov, and E. Scannapieco. Hot Atmospheres, Cold Gas, AGN Feedback and the Evolution of Early Type Galaxies: A Topical Perspective. , 215(1):5, Jan. 2019. doi: 10.1007/s11214-018-0571-9.
- R. Willingale, R. L. C. Starling, A. P. Beardmore, N. R. Tanvir, and P. T. O'Brien. Calibration of X-ray absorption in our Galaxy. , 431(1):394–404, May 2013. doi: 10.1093/mnras/stt175.



Scan the QR code to access the online version of the plots and Chandra images.

